PLEASE CITE THIS ARTICLE AS DOI: 10.1063/5.0144725

Strong collisionless coupling between an unmagnetized driver plasma and a magnetized background plasma

F. D. Cruz,[1] D. B. Schaeffer,[2] F. Cruz,[1,3] and L. O. Silva[1]

[1)] *GoLP/Instituto de Plasmas e Fusão Nuclear, Instituto Superior Técnico, Universidade de Lisboa, 1049-001 Lisboa, Portugal*

[2)] *Department of Physics and Astronomy, University of California — Los Angeles, Los Angeles, California 90095, USA*

[3)] *Inductiva Research Labs, Rua da Prata 80, 1100-420 Lisboa, Portugal*

(*Electronic mail: filipe.d.cruz@tecnico.ulisboa.pt)

(Dated: 7 April 2023)

Fast-exploding plasmas traveling though magnetized, collisionless plasmas can occur in a variety of physical systems, such as supernova remnants, coronal mass ejections, and laser-driven laboratory experiments. To study these systems, it is important to understand the coupling process between the plasmas. In this work, we develop a semi-analytical model of the parameters that characterize the strong collisionless coupling between an unmagnetized driver plasma and a uniformly and perpendicularly magnetized background plasma. In particular, we derive analytical expressions that describe the characteristic diamagnetic cavity and magnetic compression of these systems, such as their corresponding velocities, the compression ratio, and the maximum size of the cavity. The semi-analytical model is compared with collisionless 1D particle-in-cell simulations and experimental results with laser-driven plasmas. The model allows us to provide bounds for parameters that are otherwise difficult to diagnose in experiments with similar setups.

I. INTRODUCTION

Interactions between fast-expanding driver plasmas with magnetized background plasmas are commonly observed in astrophysical and space phenomena. Such examples include the interaction of stellar material with Earth's magnetosphere[1] and with the surrounding medium in supernova remnants[2], the formation of cometary plasma tails due to the solar wind[3], and artificial explosions in the Earth's upper atmosphere[4–6]. To model the physics behind these phenomena, it is important to comprehend the interaction processes between the driver and background plasmas.

This interaction can be described through the coupling, *i.e.*, the energy and momentum transfer efficiency between the driver and the background plasmas[7]. In the typical rarefied environments of astrophysical and space systems, collisions between particles are ineffective. For these collisionless processes, it is the electromagnetic fields that determine the physics of the coupling between the two plasmas[8].

A common feature of these systems is the formation of a diamagnetic cavity[9–16]. In the interaction region between the driver and the background, the electrons are magnetized while the ions are effectively unmagnetized. The resultant $\mathbf{E}\times\mathbf{B}$ electron drift leads to currents that expel the magnetic field within the driver region while compressing it at the driver's edge[7,17,18].

Many previous analytical and numerical studies on the coupling between a driver and a magnetized plasma have focused on estimating the maximum size of the diamagnetic cavity[18–22]. From energy conservation arguments, this size was calculated for sub-Alfvénic (Alfvénic Mach number $M_A < 1$)[17] and super-Alfvénic ($M_A > 1$) regimes[8,23]. By assuming hybrid models, some studies described the electric field of the system[24], while others determined the conditions where the plasmas fail to couple with each other[7]. Some attempts were also made to estimate the level of magnetic compression that results from the coupling[12,25–28].

Despite the substantial efforts in studying the coupling for these systems, it has been difficult to experimentally verify the obtained models with *in situ* observations from spacecraft, due to their limited control, data, and reproducibility. Motivated by these challenges, in recent decades, multiple scaled laboratory experiments have explored the interaction of laser-produced driver plasmas with magnetized background plasmas in collisionless regimes[24,29,30]. Some of these experiments focused on validating analytical and numerical models by measuring the size of the diamagnetic cavity for multiple parameters[12,18,20], and by exploring the electromagnetic fields of the system[15,24]. Other experiments, however, have focused on improving the momentum and energy transfer from the driver to the background and identified different regimes of coupling strength, from weak to strong coupling[31,32].

The coupling study presented in this work is motivated by recent experiments to study laboratory ion-scale magnetospheres[33] performed on the Large Plasma Device (LAPD) at the University of California—Los Angeles[34]. In these experiments, fast collisionless plasma flows generated by high-repetition-rate lasers were driven against a magnetized background plasma and a dipolar magnetic field. Under this configuration, the main characteristics of ion-scale magnetospheres were observed, and additional particle-in-cell (PIC) simulations supported the analysis of the experimental results[35]. A key component of these experiments is the initial interaction between the laser-driven plasma and background plasma; however, this interaction is difficult to diagnose directly and was limited to measurements of the magnetic field. A better model of the coupling mechanics is needed to both constrain plasma parameters that cannot be directly measured, and to predict the parameters necessary to achieve different magnetosphere regimes.

In this work, we obtain analytical expressions for multiple parameters that describe the strong coupling between a uni-

AIP Publishing Physics of Plasmas ACCEPTED MANUSCRIPT
This is the author's peer reviewed, accepted manuscript. However, the online version of record will be different from this version once it has been copyedited and typeset.
PLEASE CITE THIS ARTICLE AS DOI: 10.1063/5.0144725

form unmagnetized driver plasma and a uniform perpendicular magnetized background plasma, in non-relativistic conditions. In particular, we derive expressions for the velocities of the upstream magnetic cavity and the downstream magnetic compression, the compression ratio, and the maximum size of the cavity. The expressions for these coupling parameters are consistent with 1D PIC simulations with low electron and ion temperatures, and plasmas long enough to observe steady state-state conditions (*i.e.*, a few ion skin depths). These coupling parameters can be directly obtained from standard magnetic field diagnostics. The derived expressions could then be used to design future experiments. We also check over a limited range the validity of the coupling study against the experimental data of ion-scale magnetospheres and other LAPD experiments with laser-ablated and magnetized plasmas.

This paper is organized as follows. In Sec. II, we review the setups and results of the previous experimental and numerical ion-scale magnetosphere studies[33,35] and detail the main motivation for the coupling study. In Sec. III, we outline the configuration and parameters used to describe the system with a uniform driver flowing against a uniform magnetized background plasma. Using PIC simulations, we provide an overview of the evolution of these systems and define the parameters that best describe the coupling between the plasmas. In Sec. IV, we derive analytical expressions for these coupling parameters by using relationships from jump conditions and conservation arguments. In Sec. V, we compare these expressions with PIC simulations for scans of the magnetic field, driver density, and ion mass. We also compare the derived size of the magnetic cavity with the simulations. In Sec. VI, we apply the coupling study to experimental data. Finally, in Sec. VII, we outline the conclusions of this work.

II. MOTIVATION

The motivation for this study was a series of experiments on laboratory ion-scale magnetospheres[33]. The experiments aimed to demonstrate ion-scale magnetosphere formation using a laser-driven plasma expanding into a dipolar magnetic field, embedded in a magnetized background plasma. A key component of these experiments was energy and momentum coupling between the laser-produced plasma and the background plasma, both of which were found to play an important role in the magnetosphere formation.

The experimental platform was developed at the LAPD facility at UCLA, and details of the platform can be found in Ref. 33. A schematic of the experiments is shown in Fig. 1. In the experiments, a high-intensity laser was focused onto a solid target, releasing a fast-expanding plasma into the uniform, magnetized background plasma generated by the LAPD. A dipole magnet was inserted in the center of the background plasma and configured so that the dipolar magnetic field was parallel to the LAPD background magnetic field in the region of interest. By measuring 2D planes of the magnetic field with motorized probes, the main characteristics of ion-scale magnetospheres were identified for different magnetic moments of the dipole[33].

`Figures/LAPD_setup.pdf`

FIG. 1. Schematic setup for the laboratory ion-scale magnetosphere experiments on the LAPD. A high-intensity laser ablates a plastic target to create a supersonic plasma, which flows toward a dipole magnet. The dipole is embedded in a uniform background H plasma and magnetic field B_0 generated by the LAPD. Probes collect volumetric data from the regions around the dipole. Details on the experiments can be found in Ref. 33.

In Fig. 2, we observe the variation of the magnetic field $\Delta B_z \equiv B_z - B_{z,\mathrm{ini}}$ over time, where B_z and $B_{z,\mathrm{ini}}$ are the total and initial magnetic fields, respectively, for the cases with a) no dipole and b) a moderate dipolar magnetic moment. In c), we also observe the current density J_x for the case with a dipolar magnetic field. These results were taken along the main plasma flow direction y, in the axes of symmetry $x = z = 0$.

`Figures/experiment3.pdf`

FIG. 2. LAPD experimental results with laboratory ion-scale magnetospheres, along the symmetry axis $x = z = 0$, in the "dayside" region of the magnetosphere[33]. The dipole is centered at the origin. Evolution of the variation of the magnetic field ΔB_z for a dipolar magnetic moment of a) $M = 0$ and b) $M = 475$ Am^2. c) Current density for $M = 475$ Am^2. The LAPD background magnetic field is represented by B_0.

In the case of Fig. 2 a), there is no dipolar magnetic field present. As the driver flows against the magnetized background plasma, it expels the magnetic field in the upstream region, creating a magnetic cavity, while compressing it downstream, where the background is located. For the conditions of this experiment, the velocities of the magnetic cavity and magnetic compression are approximately constant, with values of 135 km/s and 380 km/s, respectively. We also observe that, when the driver runs out of energy, the cavity stops expanding. These results are consistent with previous LAPD experiments[13,15,18,20,27,31,32].

In Fig. 2 b), we have the case with a moderate dipolar magnetic field. At early times, the ram pressure of the laser plasma is much greater than the additional pressure from the dipolar magnetic field, and we observe the same features as in Fig. 2 a). In particular, we observe the magnetic cavity and compression moving approximately at the same velocities as in the case without a dipole. At later times as the plasma approaches the dipole magnet, there is significant additional magnetic pressure, and the plasmas are reflected, resulting in the reflection of the magnetic compression. In Fig. 2 c), we observe the current density for the same magnetic moment. We observe two current structures: the diamagnetic current, that supports the magnetic cavity in the upstream region, and the magnetopause current. These features were observed for multiple non-zero magnetic moments[33].

To explain the features in the experiments, and understand their dependency with the parameters, we performed multiple 2D PIC simulations of laboratory ion-scale magnetospheres, with a simplified setup of the experiments. Details can be found in Ref. 35. These simulations considered a uniform driver plasma flowing against a uniform, magnetized background plasma with a dipolar magnetic field located in the center. The initial setup of the simulations is represented in Fig. 3.

`Figures/sim_setup.png`

FIG. 3. Setup of the simulations with the laboratory ion-scale magnetospheres. A uniform driver plasma starts in region (I) with initial velocity v_0. The uniform background plasma starts in region (II) and has an internal magnetic field of B_0. The dipole field B_{dip} is centered at (x,y)=(0,0). Details can be found in Refs. 33 and 35.

In Fig. 4, we observe the variation of the magnetic field ΔB_z and of the current density J_x at the axis of symmetry $x = 0$, for a simulation in similar conditions to the experiment in Fig. 2 b).

`Figures/standard.pdf`

FIG. 4. Temporal evolution of (a) the variation of the magnetic field ΔB_z and (b) the current density J_x at the symmetry axis $x = 0$, in the "dayside" region, for a simulation of laboratory ion-scale magnetospheres in similar conditions to the experiment in Fig. 2 b).

Similar to the experimental plot in Fig. 2 b), Fig. 4 a) shows the formation of a magnetic cavity upstream and a magnetic compression downstream, in the initial times of the simulation, where the dipole is negligible. The plasmas continue to approach the dipole until the magnetic field is strong enough to reflect the magnetic compression. The simulations also showed that the observation of this reflection depends on the size of the driver, *i.e.*, it cannot be too short along y, or the driver will not have enough energy to reach near the dipole, nor it can be too large, or the late decompression of the background (after $t\omega_{ci} \approx 5$ in Fig. 4) will occur before the driver reflection[35].

Fig. 4 b) shows the current density J_x of the simulation. Similarly to Fig. 2 c), we observe two main current structures, namely, the diamagnetic current and the magnetopause current. The standoff locations for these currents can be estimated by the pressure balance between the ram pressure exerted by the plasmas and the magnetic field pressure

$$n m_i v_0^2 = \frac{B_z^2}{8\pi} , \tag{1}$$

where n, m_i, and v_0 represent the ion density, mass, and fluid velocity of the plasma. We observed that the magnetopause current is more easily identified for low magnetic moments and that it is supported by the background and driver plasmas with some time dependence. These results were also consistent with the experiments[33,35].

Since the plasmas interact with each other before being stopped by the dipole at the standoff distance, the features observed in the experimental and numerical studies of laboratory ion-scale magnetospheres are dependent on the coupling strength between the two plasmas. The densities affect this coupling[7], leading to faster magnetic cavities for higher driver densities, which results in different magnetospheric features[35]. Additionally, even without the dipole, the driver continuously loses energy to the background and eventually stops expanding, as seen in Fig. 2 a). To observe the reflection of the magnetic compression, we need to ensure that the driver has enough energy to reach the standoff distance, which depends on the coupling[8,17,35].

To better understand and design experiments with laboratory ion-scale magnetospheres, we then need to accurately describe the coupling of the system. In Secs. III to V, we present a model capable of describing this coupling, for a range of parameters relevant to current experimental facilities.

III. PIC SIMULATIONS

A. Configuration of the simulations

To study the coupling between an unmagnetized driver plasma and a magnetized background plasma, we performed multiple 1D simulations with OSIRIS, a massively parallel and fully relativistic PIC code[36,37]. With PIC simulations, we can accurately resolve the plasma kinetic scales of these systems.

The simulations consist of a 25 d_i length region with open boundary conditions at $y = -5\ d_i$ and $y = 20\ d_i$, where $d_i = c/\omega_{pi} = \sqrt{m_{i,0}c/4\pi n_0 e^2}$ is the ion skin depth of the background plasma, with c the speed of light in vacuum, ω_{pi} the ion plasma frequency, e the electron charge, and $m_{i,0}$ and n_0 the ion mass and the density of the background plasma, respectively. To resolve the dynamics of the electron kinetic scales, we used 10 grid cells per electron skin depth $d_e = d_i\sqrt{m_e/m_{i,0}}$, where m_e is the electron mass.

For the driver plasma, the simulations consider an idealized and simplified configuration when compared to typically laser-produced driver plasmas in the laboratory[15,38]. In the experiments, the initial fast driver has a much higher ion gyroradius than the background ions, so we can consider the driver as unmagnetized and well-separated from the background. The driver has an initial fluid velocity $\mathbf{v_0} = v_0\ \hat{\mathbf{y}}$, a uniform density n_d, and a length $L_y = 5\ d_i$. The driver is initially located between $y = -5\ d_i$ and $y = 0$, and it is composed of electrons and a single species of ions with mass $m_{i,d}$. Equivalently, the background plasma has a density of n_0 and a length of $L_B = 20\ d_i$. It is located between $y = 0$ and $y = 20\ d_i$, and it is also composed of electrons and a single species of ions with mass $m_{i,0}$. Unlike the driver, the background plasma is magnetized by an internal and uniform magnetic field $\mathbf{B_0} = B_0\ \hat{\mathbf{z}}$. The magnitude B_0 is calculated from the Alfvénic Mach number, defined as $M_A \equiv v_0/v_A = v_0\sqrt{4\pi n_0 m_{i,0}}/B_0$, where v_A is the Alfvén velocity. Both plasmas have 200 particles per cell per species and ions with charge $q_i = e$.

We consider electron thermal velocities of $v_{the} = 0.1\ v_0$, with $v_{the,x} = v_{the,y} = v_{the,z} = v_{the}/\sqrt{3}$, and that the ions and electrons are initially in thermal equilibrium. Since the most relevant dynamics of the simulations occur at the ion kinetic scales, the spatial scales are normalized to d_i and the time scales to the ion cyclotron gyroperiod of the background plasma $\omega_{ci}^{-1} = m_{i,0}c/eB_0$.

The simulations consider colder plasmas, lower ion mass ratios $m_{i,0}/m_e = 100$, and faster fluid velocities $v_0 = 0.1\ c$ than expected in experiments and most space and astrophysical scenarios. These approximations reduce the computational resources necessary to perform the simulations, allow extended scans over different parameters, and simplify our analysis. The chosen ion-to-electron mass ratio in the simulations is high enough to ensure sufficient separation between electron and ion spatial and temporal scales.

Additionally, n_0 is the independent variable of OSIRIS. We ensure that v_0 is low enough to neglect relativistic effects on the system. By using proper space and time scales (d_i, ω_{ci}^{-1}), we expect the main properties of the system to scale with the main dimensionless parameters (M_A, n_d/n_0, and $m_{i,d}/m_{i,0}$). By using similar dimensionless quantities for both the experiments and simulations, the simplifications considered should not affect the main results.

The main parameter scans presented in this paper consider $0.2 \leq n_d/n_0 \leq 10$, $1 \leq m_{i,d}/m_{i,0} \leq 9$ and low Alfvénic Mach numbers such that $0.5 \leq M_A \leq 1.5$. These ranges were chosen due to their relevance to LAPD laser experiments. Later simulations also consider high Mach numbers $2 \leq M_A \leq 10$ and longer plasmas with $L_y = 120\ d_i$ and $L_B = 300\ d_i$. During the parameter scans, we keep the background parameters n_0 and $m_{i,0}$ unchanged, and instead change the driver parameters n_d and $m_{i,d}$, and the Mach number M_A. For these parameters, and for the density profiles considered, the lengths and times of the simulations are long enough to observe a quasi-steady-state regime of the system for a sufficient amount of time[25] and a strong coupling regime between the two plasmas[32].

B. Basic system dynamics

Fig. 5 illustrates the basic temporal evolution of the system and shows the ion densities n_i of the driver and background plasmas, the ion phase spaces, and the magnetic field B_z, for three different times. The initial setup of the simulations is shown in Figs. 5 a1) and b1). The simulation represented considers $n_d/n_0 = 2$, $m_{i,d}/m_{i,0} = 1$, and $M_A = 1.5$.

We see in Figs. 5 a1–4) that, as the driver flows to the right, it pushes the background plasma and the magnetic field with it, leading to a relocation of the interface between the two plasmas and creating two high-density regions on both sides of the interface. During this process, the driver ions are mostly confined in the upstream region relative to the plasma flow, while the background ions are mostly confined downstream, with the exception of small amounts of the driver and background ions that entered the opposite regions in the initial times of the simulation[40,41].

The magnetic field rapidly increases in the transition from the unmagnetized driver to the magnetized background, as we can see in Figs. 5 b1–4). Due to the large mass discrepancies

Physics of Plasmas ACCEPTED MANUSCRIPT

This is the author's peer reviewed, accepted manuscript. However, the online version of record will be different from this version once it has been copyedited and typeset.

PLEASE CITE THIS ARTICLE AS DOI: 10.1063/5.0144725

AIP Publishing

`Figures/basic-coupling.pdf`

FIG. 5. a) Ion densities n_i and b) y component of the ion velocities v_y, for the driver (orange) and background (blue) plasmas. The green line shows the magnetic field B_z. Columns 1–4 correspond to four different times. The simulation considers $n_d/n_0 = 2$, $m_{i,d}/m_{i,0} = 1$, and $M_A = 1.5$. [Associated dataset available at https://zenodo.org/record/7485077 (Ref. 39).]

between the electrons and the ions, the transition occurs over a length scale larger than the local electron gyroradius but much smaller than the local ion gyroradius, and so, in the interface region between the two plasmas, the driver electrons are effectively magnetized while the driver ions are unmagnetized. The space-charge separation creates a negative electric field in the y direction that reflects the driver ions back upstream with a new velocity $v_1 < v_0$, and causes an electron $\mathbf{E} \times \mathbf{B}$ drift, which leads to a diamagnetic current. This current expels the magnetic field upstream, creating a magnetic cavity with no magnetic field, while the field is compressed downstream[13,17,18]. A more detailed study of the electric fields of the transition region is presented in Appendix A.

The energy and momentum lost by the driver plasma during this process are transferred to the background region. The initially stationary background ions are accelerated and the

AIP Publishing Physics of Plasmas ACCEPTED MANUSCRIPT
This is the author's peer reviewed, accepted manuscript. However, the online version of record will be different from this version once it has been copyedited and typeset.
PLEASE CITE THIS ARTICLE AS DOI: 10.1063/5.0144725

magnetic field is compressed. From this interaction, the bulk of the driver, the compressed background, and the interface between the plasmas travel to the right through the region initially occupied by the background plasma. Additionally, during this process, multiple waves and instabilities form in the background region, as we see in Fig. 5 b3). We also observe that the size of the perturbed background region increases over time.

In Fig. 5, the magnetic field and the plasma densities of the system are not constant, however, some average quantities of the system do not change significantly over time. Such examples include the average velocity of the accelerated background ions and the average of the compressed magnetic field. We could, therefore, consider that the system achieves a quasi-steady-state regime and that it can be represented by its average properties, as we show in Sec. IV.

C. Magnetic field diagnostics

To comprehend the dynamics of these systems, it is important to investigate the evolution of the magnetic field B_z since it can be used to determine the motion of the particles and the electric fields. Additionally, magnetic field diagnostics are widely used for fast-driven plasmas in laboratory experiments[15,18,33]. From Ampère's law, the x component of the current density is $J_x \approx (c/4\pi)\cdot\partial B_z/\partial y$, and so, we can use J_x to investigate changes in the magnetic field.

To illustrate these two important quantities, we show in Fig. 6 the temporal evolution of a) the variation of the magnetic field $\Delta B_z \equiv B_z - B_{z,\text{ini}}$, where $B_{z,\text{ini}}$ is the initial magnetic field, and b) the current density J_x. To understand how the system depends on the initial parameters, these diagnostics are shown for three driver densities: 1) $n_d/n_0 = 0.5$, 2) $n_d/n_0 = 2$, and 3) $n_d/n_0 = 5$, with $m_{i,d}/m_{i,0} = 1$ and $M_A = 1.5$.

In Fig. 6 we observe the same main structures for the three driver densities. Similarly to the experiment in Fig. 2 a), and as discussed in Sec. III B, while the driver flows against the background, it expels the magnetic field, creating a magnetic cavity, as observed in Figs. 6 a1–3). Due to the initial uniformity of the system, the magnetic cavity has essentially no magnetic field. This magnetic cavity expands over time, and its maximum extent increases with the driver density. This is expected since the energy and the pressure exerted by the driver increase with its density, improving the coupling between the plasmas[7]. The velocity at which the magnetic cavity travels through the background is designated by coupling velocity v_c. This velocity is always lower than v_0 and increases with the driver density, as shown in Fig. 6.

After all the driver ions with velocity v_0 are reflected, the driver may not have enough energy to push the background any further, leading to the reflection of the magnetic cavity. This happens for $n_d/n_0 = 0.5$ and $n_d/n_0 = 2$ (at $t\omega_{ci} \approx 5$ and $t\omega_{ci} \approx 8$, respectively). This is also represented in Fig. 5 b4). For $n_d/n_0 = 5$, the reflected driver ions with velocity v_1 have still enough momentum to continue pushing the magnetic cavity through the background region, although at a lower velocity. We consider the stopping distance L_stop the distance that the magnetic cavity travels before the driver ions with velocity v_0 are fully reflected, *i.e.*, during the main interaction of the system. For $n_d/n_0 = 5$, the stopping distance would then be $L_\text{stop} \approx 10.4\ d_i$.

In Figs. 6 a1–3), we also observe the magnetic compression in the downstream region, where the background is located. While the compressed magnetic field is not constant, its average does not change significantly over time during the main interaction of the plasmas. The average ratio of compressed to the initial magnetic field is designated by compression ratio α. Additionally, the extent of the background plasma with compressed magnetic field increases over time. The velocity at which the magnetic compression travels through the unperturbed background plasma is designated by front velocity v_f. Fig. 6 shows that v_f also increases with the driver density. After the driver's reflection, the compressed plasma continues to move through the unperturbed background.

Figs. 6 b1–3) show the current densities for the different driver densities. The sudden increase in magnetic field from the magnetic cavity to the magnetized background plasma is supported by the diamagnetic current[13]. In the background region, we also observe multiple current structures associated with the fast and slow magnetosonic (MS) waves that form in the background plasma[15,28].

IV. COUPLING PARAMETERS

As discussed in Sec. III B, for uniform densities, and if the plasmas are long enough, the system reaches a quasi-steady-state regime, where some average quantities do not change significantly over time. Under these conditions and assuming the MHD formalism, we can describe the system by three different regions with different magnetic and kinetic properties, as shown in Fig. 7.

The first region in Fig. 7 refers to the magnetic cavity, where $B_z \approx 0$. The driver plasma is located in this upstream region, and the ion motion of the driver can be described by two ion populations with velocities $\mathbf{v_0}$ and $\mathbf{v_1}$. The second region refers to the magnetic compression, where the average magnetic field is αB_0. In this region, the background ions accelerated by the interaction with the driver plasma have an average velocity of $\mathbf{v_m}$. Finally, the third region refers to the background region that remains unperturbed by the interaction of the two plasmas. Here, the magnetic field is B_0 and the background ions have no flow velocity. These three regions are visible in Fig. 6.

The regions are separated by two discontinuities where the plasma properties change abruptly. Discontinuities A and B move through the simulation box with velocity $\mathbf{v_c}$ and $\mathbf{v_f}$, respectively. Some physical quantities must be conserved from the upstream to the downstream side of the discontinuities. With these conservation laws, we can derive analytical expressions for the coupling parameters α, v_c, and v_f. In the context of classical MHD classification of discontinuities, and from the simple description of the system in Fig. 7, discontinuity A is a tangential discontinuity, because there is no plasma flow through its surface and the magnetic field is parallel to the sur-

AIP Publishing

Physics of Plasmas ACCEPTED MANUSCRIPT

This is the author's peer reviewed, accepted manuscript. However, the online version of record will be different from this version once it has been copyedited and typeset.

PLEASE CITE THIS ARTICLE AS DOI: 10.1063/5.0144725

`Figures/standard_coupling_high2.pdf`

FIG. 6. Temporal evolution of a) the variation of the magnetic field ΔB_z and b) the current density J_x for three different simulations with 1) $n_d/n_0 = 0.5$, 2) $n_d/n_0 = 2$, and 3) $n_d/n_0 = 5$, with $m_{i,d}/m_{i,0} = 1$ and $M_A = 1.5$. The dotted line has a slope equal to v_0, and the dashed lines have slopes equal to the coupling velocity v_c and the front velocity v_f. Frames a2) and b2) correspond to the simulation shown in Fig. 5. We observe magnetosonic (MS) waves in the background in all frames.

face, and discontinuity B corresponds to a forward fast-mode shock[42].

A. Jump conditions at the discontinuities

To derive expressions for the coupling parameters, we consider the system description in Fig. 7. In the reference frame of the discontinuities, and for a quasi-steady-state regime, the time derivatives can be dropped in the MHD and Maxwell's equations.

In the upstream and downstream sides of each discontinuity, some physical quantities must be conserved, which leads to the Rankine-Hugoniot (R-H) jump conditions. We can consider the experiments and simulations with ion-scale magnetospheres as collisionless[33,35], so we can ignore collisions in

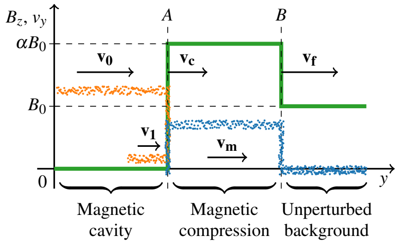

FIG. 7. Simplified representation of the interaction between the flowing driver (orange) with the background (blue) and the magnetic field profile (green). All quantities represented are measured in the lab frame. The dots illustrate the plasma particles' velocities. This model considers three regions: the magnetic cavity, the magnetic compression, and the unperturbed background. These regions are separated by the discontinuities A and B.

the R-H jump conditions. For magnetic fields perpendicular to the plasma flows, these conditions lead to[43–46]

$$[vB] = 0 \tag{2a}$$

$$[n_i v] = 0 \tag{2b}$$

$$\left[n_i m_i v^2 + p + \frac{B^2}{8\pi} \right] = 0 \tag{2c}$$

$$\left[n_i m_i v \left(\frac{1}{2} v^2 + u + \frac{p + B^2/8\pi}{n_i m_i} \right) \right] = 0 \, . \tag{2d}$$

In the previous equations, $[X] \equiv X_1 - X_2$ stands for the difference of values of a quantity X in the upstream and downstream regions, while n_i, m_i, and v stand for the density, mass, and velocity of the ions, respectively, p for the electron pressure, u for the internal energy per unit mass, and B for the magnetic field. Eq. (2a) corresponds to Ohm's law, and Eqs. (2b) to (2d) to the mass, momentum, and energy conservation laws. We can apply these equations to both discontinuities A and B in Fig. 7.

B. R-H equations at discontinuity A

From Eq. (2a), the quantity $v_y B_z$ must be conserved in the reference frame of discontinuity A. This leads to

$$(v_m - v_c)\alpha B_0 = 0 \Longrightarrow v_m = v_c \, . \tag{3}$$

By also applying Eqs. (2b) and (2d) to the discontinuity, we obtain

$$n_d m_{i,d}(v_0 - v_c) + n'_d m_{i,d}(v_1 - v_c) = 0 \tag{4}$$

$$\frac{1}{2}(v_0 - v_c)^2 - \frac{1}{2}(v_1 - v_c)^2 + u_d - u'_d + \frac{p_d}{n_d m_{i,d}} - \frac{p'_d}{n'_d m_{i,d}} = 0 \, , \tag{5}$$

where n'_d, p'_d, and u'_d are the density, pressure, and internal energy density of the driver population with velocity v_1. If we assume similar thermal properties for the two driver populations, the enthalpy terms $w = u + p/nm$ in Eq. (5) cancel out. This was consistently observed for the simulations in this paper, with low electron and ion thermal velocities. Eqs. (4) and (5) then lead to $n'_d = n_d$ and $v_c = (v_0 + v_1)/2$, as expected.

Finally, from Eq. (2c), the momentum must also be conserved, which leads to

$$2 n_d m_{i,d}(v_0 - v_c)^2 + p_d + p'_d = p_2 + \frac{(\alpha B_0)^2}{8\pi}$$

$$\Longrightarrow \left(\frac{M_A}{R_n} \right)^2 \left(1 - \frac{v_c}{v_0} \right)^2 = \alpha^2 + \beta_2 - \beta_d \, , \tag{6}$$

where the factor of 2 considers both populations of driver ions with v_0 and v_1 velocities, p_2 corresponds to the electron pressure in the compressed background region, and $\beta_d \equiv 8\pi(p_d + p'_d)/B_0^2$, $\beta_2 \equiv 8\pi p_2/B_0^2$, and

$$R_n \equiv \frac{1}{2} \left(\frac{n_0}{n_d} \frac{m_{i,0}}{m_{i,d}} \right)^{\frac{1}{2}} \, . \tag{7}$$

To determine the other equations for the coupling parameters, we now apply Eqs. (2a) to (2d) to discontinuity B.

C. R-H equations at discontinuity B

By applying Eqs. (2a) and (2b) to the reference frame of discontinuity B, we obtain

$$(v_m - v_f)\alpha B_0 = -v_f B_0 \Longrightarrow \alpha = \frac{v_f}{v_f - v_c} \tag{8}$$

$$(v_m - v_f) n_2 = -v_f n_0 \Longrightarrow \alpha = \frac{n_2}{n_0} \, , \tag{9}$$

where n_2 refers to the density of the compressed background plasma. Eqs. (8) and (9) show that the background density and magnetic field increase by the same ratio[28,32]. Eq. (8) also shows a dependency between the three coupling parameters α, v_c, and v_f.

Using Eq. (2c), we have from the momentum conservation in B that

$$\alpha n_0 m_{i,0} \left(\frac{v_f}{\alpha} \right)^2 + p_2 + \frac{(\alpha B_0)^2}{8\pi} = n_0 m_{i,0} v_f^2 + p_1 + \frac{B_0^2}{8\pi}$$

$$\Longrightarrow \beta_2 = \beta_1 + (1 - \alpha^2) + 2 M_B^2 \left(1 - \frac{1}{\alpha} \right) \, , \tag{10}$$

where p_1 is the initial background electron pressure, $\beta_1 \equiv 8\pi p_1/B_0^2$, and $M_B \equiv v_f/v_A$. With Eq. (2d) and using $u = p/(\gamma - 1) n_i m_i$, where γ is the adiabatic index, we obtain

$$M_B^2 \left(1 - \frac{1}{\alpha^2} \right) + \frac{\gamma}{(\gamma - 1)} \left(\beta_1 - \frac{\beta_2}{\alpha} \right) + 2(1 - \alpha) = 0 \, . \tag{11}$$

Finally, Eqs. (10) and (11) allow us to derive an expression for the compression ratio[26,28,43,46]

AIP Publishing Physics of Plasmas ACCEPTED MANUSCRIPT

This is the author's peer reviewed, accepted manuscript. However, the online version of record will be different from this version once it has been copyedited and typeset.
PLEASE CITE THIS ARTICLE AS DOI: 10.1063/5.0144725

$$\alpha = \frac{2(\gamma+1)}{\gamma-1}\left[1+\frac{\gamma(1+\beta_1)}{\gamma-1}M_B^{-2}+\left(\left[1+\frac{\gamma(1+\beta_1)}{\gamma-1}M_B^{-2}\right]^2+4\frac{(1+\gamma)(2-\gamma)}{(\gamma-1)^2}M_B^{-2}\right)^{1/2}\right]^{-1} . \tag{12}$$

Eq. (12) shows an expression for α as a function of the velocity of the discontinuity. By solving Eqs. (6), (8), and (12) numerically, we can determine the coupling parameters α, v_c, and v_f with only the initial conditions of the system.

D. Solutions for low Mach numbers

With Eqs. (6) and (12), and by using Eq. (10) to replace β_2 in Eq. (8), we obtain a set of three equations that relate the coupling parameters α, v_c, and v_f with each other and with the initial parameters of the system. By solving these equations numerically, we can calculate these parameters for given initial conditions. In some regimes, however, it is possible to also obtain analytical expressions for the coupling parameters.

From Eq. (12), it can be shown that for cold plasmas, such that $\beta_1, \beta_d \ll 1$, and low Mach numbers, we can consider $\alpha \approx M_B \equiv v_f/v_A$ (see Appendix B). Replacing Eq. (12) by this approximation, and using Eqs. (6) and (8), we have that α, v_c, and v_f are given by

$$\alpha = \frac{1+M_A}{1+R_n} \tag{13a}$$

$$\frac{v_c}{v_0} = \frac{1}{M_A}\frac{M_A-R_n}{1+R_n} \tag{13b}$$

$$\frac{v_f}{v_0} = \frac{1}{M_A}\frac{1+M_A}{1+R_n} . \tag{13c}$$

These expressions depend only on the initial parameters of the system. We stress that α, v_c, and v_f can be directly measured from the magnetic diagnostics of the experiments and of the simulations, and therefore, they can be used to evaluate the coupling between the plasmas and to estimate uncertain initial conditions of the system.

The equations shown here are only valid for the main interaction of the system, *i.e.*, before all the driver ions get reflected. After the main interaction, these reflected ions may still have enough energy to continue pushing the background forward, creating a second interaction between the driver and the background, but with different parameters.

E. Solutions for high Mach numbers

We can also obtain analytical expressions for the coupling parameters for cold plasmas and high Mach numbers, such that $\beta_1, \beta_d \ll 1$ and $M_A \gg 1$. Under this conditions, Eqs. (6), (8), and (12) lead to

$$\alpha = \frac{\gamma+1}{\gamma-1} \tag{14a}$$

$$\frac{v_c}{v_0} = \frac{1}{1+R_n\sqrt{1+\gamma}} \tag{14b}$$

$$\frac{v_f}{v_0} = \frac{1+\gamma}{2(1+R_n\sqrt{1+\gamma})} . \tag{14c}$$

Eq. (14a) represents the maximum value for the compression ratio, well-known in strong shock theory[43,44,46].

V. COMPARISON BETWEEN THE EQUATIONS AND THE SIMULATIONS

A. Dependency on the driver density

After deriving analytical expressions that describe the coupling between the driver and background plasmas, we now verify the validity of Eqs. (13a) to (13c). We are interested in the cases where $M_A \sim 1$ and $n_d \sim n_0$ for the experiments with ion-scale magnetospheres[33,47]. For these conditions, we can apply the solutions for low Mach numbers, represented in Sec. IV D.

Fig. 8 shows the measured values for the coupling parameter ratios α, v_c/v_0, and v_f/v_0, for multiple simulations with different Alfvénic Mach numbers M_A and driver-to-background density ratios n_d/n_0, with $m_{i,d}/m_{i,0} = 1$. The measured coupling parameters are plotted alongside the values calculated with Eqs. (13a) to (13c). The uncertainties for the measurements of the coupling parameters are negligible (typically less than 2%).

Fig. 8 confirms that Eqs. (13a) to (13c) can be used to describe the coupling of the system, for the regimes considered. In Fig. 8 a) we observe that the magnetic compression ratio α increases with the driver density and the Mach number, since for these conditions, the magnetic field offers less resistance to the driver, leading to tighter compressions. The parameter α was measured by first averaging spatially the compressed background magnetic field for each time, and then by averaging these values temporally. We can also see for three of the simulations ($M_A = 0.5$ and $n_d/n_0 = 0.5$, $M_A = 0.75$ and $n_d/n_0 = 0.2$, and $M_A = 0.75$ and $n_d/n_0 = 0.4$), that the driver is not capable of compressing the background, leading to a magnetic decompression with $\alpha < 1$.

In Fig. 8 b), the measured coupling velocities v_c of the simulations are consistent with Eq. (13b). Similarly to the magnetic compression ratio, v_c increases with the driver density and the Mach number. For the three simulations with $\alpha < 1$, we observe negative coupling velocities, meaning that the driver is pushed back by the background and that it is the

`Figures/coupling-density-scan-ea.pdf`

FIG. 8. Comparison between the coupling parameters measured in the simulations for a) α with Eq. (13a), b) v_c/v_0 with Eq. (13b), and c) v_f/v_0 with Eq. (13c), for different M_A and n_d/n_0 values. These simulations considered $m_{i,d}/m_{i,0} = 1$. The coupling parameters measured in the simulations are represented by dots and the analytical expressions by dashed lines. [Associated dataset available at https://zenodo.org/record/7485077 (Ref. 39).]

`Figures/coupling-mass-scan.pdf`

FIG. 9. Comparison between the coupling parameters measured in the simulations for a) α with Eq. (13a), b) v_c/v_0 with Eq. (13b), and c) v_f/v_0 with Eq. (13c), for different M_A and $m_{i,d}/m_{i,0}$ values. These simulations considered $n_d/n_0 = 1$. The coupling parameters measured in the simulations are represented by dots and the analytical expressions by dashed lines. [Associated dataset available at https://zenodo.org/record/7485077 (Ref. 39).]

background that transfers its energy and momentum to the driver plasma.

Finally, in Fig. 8 c), we see that the front velocity v_f increases with the driver density but decreases with the Mach number. For low Mach numbers, we observe small discrepancies between the simulations and Eq. (13c). These differences are mostly associated with the overestimation of the front velocity by Eq. (13c). When measuring v_f, some caution was also required for the simulations with low magnetic compressions, *i.e.*, $\alpha \approx 1$, and due to the presence of waves in the background plasma (see the background magnetosonic waves in Fig. 5).

B. Dependency on the driver ion mass

To continue the validation of Eqs. (13a) to (13c), we now compare them in Fig. 9 to simulations with different driver-to-background ion mass ratios $m_{i,d}/m_{i,0}$ and different Alfvénic Mach numbers M_A. The simulations consider $n_d/n_0 = 1$. To ensure that the ion masses were high enough to separate the electron spatial and temporal scales from the ions, no sub-unit ion mass ratio was tested (*i.e.*, $m_i/m_e \geq 100$).

Similarly to Fig. 8, the results of simulations with different ion masses are consistent with Eqs. (13a) to (13c). Once again, Eq. (13c) overestimates the front velocities measured in the simulations for low Mach numbers, mainly due to the difficulty in measuring v_f in these simulations. After comparing the measured coupling parameters with Eqs. (13a) to (13c) for low Mach numbers, we now compare the derived solutions for high Mach numbers in Sec. V C.

C. Solutions for high Mach numbers

To study the coupling for higher Mach numbers, we performed additional simulations with $2 \leq M_A \leq 10$. To ensure that a quasi-steady-state was observed in these regimes and that we could measure α with a sufficiently large compressed background region, we considered longer plasmas for these new simulations, namely $L_y = 120\ d_i$ for the driver and $L_B = 300\ d_i$ for the background. Due to computational limitations, the background plasma is not large enough for all the measurements of the stopping distance.

Fig. 10 compares the different solutions obtained for the coupling parameters α, v_c/v_0, and v_f/v_0, with the values measured in the simulations, for multiple Mach numbers M_A, and the density ratios $n_d/n_0 = 0.2$, 1, and 5. The simulations represented considered $m_{i,d}/m_{i,0} = 1$. Since the background magnetic field is aligned along z, the heat flow should only be negligible in the x and y directions. As a result, the solutions presented in Fig. 10 consider $\gamma = 2$ for the perpendicularly magnetized background plasma[48–50].

As we can observe in Fig. 10, the coupling parameters measured in the simulations are consistent with the solutions obtained by numerically solving Eqs. (6), (8), and (12). As expected, Eqs. (13a) to (13c) are also consistent with the numerical solutions for low Mach numbers, while Eqs. (14a) to (14c)

Figures/coupling-high-scan.pdf

FIG. 10. Comparison between the coupling parameters a) α, b) v_c/v_0, and c) v_f/v_0, measured in the simulations and calculated with the solutions obtained in Sec. IV. The simulations with $M_A < 2$ consider $L_y = 5\ d_i$ and $L_B = 20\ d_i$, while the simulations with $M_A \geq 2$ consider $L_y = 120\ d_i$ and $L_B = 300\ d_i$. The simulations are represented by dots and considered $m_{i,d}/m_{i,0} = 1$. The dashed lines correspond to the solutions obtained by numerically solving Eqs. (6), (8), and (12). The dash-dotted lines correspond to the solutions for low Mach numbers, calculated with Eqs. (13a) to (13c), and the dotted lines to the solutions for high Mach numbers, calculated with Eqs. (14a) to (14c). The solid lines in a) correspond to the analytical solutions for α when using Eq. (12), $M_B = M_A v_f/v_0$, and Eq. (13c). All solutions considered $\gamma = 2$.

are consistent for high Mach numbers. For $\gamma = 2$ and $M_A \gg 1$, the magnetic compression saturates in $\alpha \approx 3$.

In Fig. 10 c) we also observe that Eq. (13c), the analytical solution for the front velocity v_f and low Mach numbers M_A, is similar to the numerical solution and the values measured in the simulations for both low and high Mach numbers, in particular, for the lower density ratios. If we then calculate $M_B = M_A v_f/v_0$ with Eq. (13c), the approximation of v_f/v_0 for low Mach numbers, such that

$$M_B \equiv \frac{v_f}{v_A} \approx \frac{1+M_A}{1+R_n} , \tag{15}$$

and replace it in Eq. (12), we obtain an additional analytical solution for α that works for both the low and high Mach number regimes. As we can see in Fig. 10 a) with the solid lines, this new analytical solution is a good approximation to the values measured in the simulations and in the numerical solutions.

After confirming that we can describe the coupling between the plasmas with the initial parameters of the system, both analytically and numerically, we can now use the obtained solutions to evaluate other characteristics of the system.

D. Stopping distance of the magnetic cavity

Figs. 8, 9, and 10 showed that we can use Eqs. (13a) to (13c) and Eqs. (14a) to (14c) to describe how the system evolves over time, for low and high Mach numbers, respectively. These equations are also useful to obtain other parameters, such as the stopping distance L_{stop}, *i.e.*, the maximum distance that the magnetic cavity can travel through the background region, during the main interaction of the system.

The reflection time of the magnetic cavity also corresponds to the reflection time of the driver by the background plasma. The magnetic cavity travels a distance L_{stop} through the background region, with velocity v_c, while the driver, with a length L_y, travels with a velocity $v_0 - v_c$, relative to the driver-background boundary. The magnetic cavity will travel a distance L_{stop} after a time L_{stop}/v_c, and all the driver ions with velocity v_0 will be reflected after a time $L_y/(v_0 - v_c)$. By balancing the two time intervals, we obtain that the stopping distance can then be described by

$$L_{\text{stop}} = L_y \frac{v_c}{v_0 - v_c} . \tag{16}$$

Previously derived expressions for the stopping distance only consider the driver energy transfer to the magnetic field, for sub-Alfvénic regimes[12,17,22,23,27], or the driver energy transfer to the background kinetic energy, for super-Alfvénic regimes[8,23,27]. On the contrary, Eq. (16) considers both the background kinetic and magnetic energy transfers, but also, the energy of the reflected driver particles with velocity v_1 (*i.e.*, not all the driver energy is transferred to the background). By using Eq. (13b) for low Mach numbers, the stopping distance becomes

$$L_{\text{stop}} = L_y \frac{M_A - R_n}{R_n(1+M_A)} . \tag{17}$$

Fig. 11 compares Eq. (17) with the measured stopping distance L_{stop} in the simulations. Fig. 11 a) shows the results for different driver-to-background density ratios n_d/n_0 and different Alfvénic Mach numbers M_A, with $m_{i,d}/m_{i,0} = 1$, and Fig. 11 b) for different driver-to-background ions mass ratios $m_{i,d}/m_{i,0}$ and M_A, with $n_d/n_0 = 1$.

Figs. 11 a) and b) show good agreement between Eq. (17) and the stopping distances measured in the simulations. For high densities and mass ratios, and Mach numbers around $M_A \sim 1.5$, Eq. (17) overestimates the stopping distances. As we observed in Fig. 8 b) and Fig. 9 b), for these parameters, the coupling velocity is close to v_0. Since the stopping distance is proportional to $v_c/(v_0 - v_c)$, small discrepancies between Eq. (13b) and the simulations may lead to large differences in the L_{stop} values, for these conditions. To accurately calculate the stopping distance for higher Mach numbers, the full numerical solution must be used.

For high Mach numbers, and using Eq. (14b), the stopping distance is given by

$$L_{\text{stop}} = \frac{L_y}{R_n\sqrt{1+\gamma}} . \tag{18}$$

AIP Publishing Physics of Plasmas ACCEPTED MANUSCRIPT

This is the author's peer reviewed, accepted manuscript. However, the online version of record will be different from this version once it has been copyedited and typeset.

PLEASE CITE THIS ARTICLE AS DOI: 10.1063/5.0144725

`Figures/stopping-scan.pdf`

FIG. 11. Comparison between the stopping distance L_{stop} measured for multiple simulations, with the uncertainty represented by the errorbars, and calculated with Eq. (17), by the dashed lines. The upper and lower errorbars have equal size and account for the non-sharp magnetic cavity reflection in some simulations. a) Scan for different driver-to-background density ratios n_d/n_0 and Alfvénic Mach numbers M_A, with $m_{i,d}/m_{i,0} = 1$. b) Scan for different M_A and driver-to-background ion mass ratios $m_{i,d}/m_{i,0}$, with $n_d/n_0 = 1$. [Associated dataset available at https://zenodo.org/record/7485077 (Ref. 39).]

`Figures/stopping-scan-high.pdf`

FIG. 12. Comparison between the stopping distance L_{stop} measured for multiple simulations, with the uncertainty represented by the errorbars, and Eq. (16). The errorbars account for the non-sharp magnetic cavity reflection and the formation of a "foot" structure in the driver-background interface in some simulations. The dashed lines correspond to values calculated with Eq. (16) and the numerical solutions of v_c, the dash-dotted lines to the low Mach number solution of Eq. (17), and the dotted lines to the high Mach number solution of Eq. (18). The simulations considered different driver-to-background density ratios n_d/n_0 and Alfvénic Mach numbers M_A, with $m_{i,d}/m_{i,0} = 1$. The simulations used a driver length of $L_y = 5\ d_i$, for $M_A < 2$, and $L_y = 120\ d_i$, for $M_A \geq 2$.

To also validate the solutions for high Mach numbers, Fig. 12 compares the values measured in the simulations with the obtained solutions for the different Mach number regimes. The simulations consider $m_{i,d}/m_{i,0} = 1$ and the density ratios $n_d/n_0 = 0.2$ and 1.

Similarly to Fig. 10, Fig. 12 shows that the stopping distance L_{stop} calculated with Eq. (16) and the numerical solutions of v_c are consistent with the values measured in the simulations, from low to high Mach numbers. Additionally, Eq. (17) is consistent with the simulations for low Mach numbers, while Eq. (18) is consistent with the simulations for high Mach numbers. As previously seen in Fig. 11, Eq. (17) may overestimate the stopping distances, even in the low Mach number $M_A \sim 1$ regime. In some of the high M_A simulations, some "foot" structures were observed in the driver-background interface, leading to some uncertainty in the measured values of the stopping distance.

VI. APPLICATIONS TO EXPERIMENTS

Eqs. (13a) to (13c) relate the different coupling parameters with the initial conditions of the system, for the low Mach numbers expected for the experiments with ion-scale magnetospheres. Having a model capable of relating these parameters in experiments with laser-ablated and magnetized background plasmas will help us understand the energy transfer efficiency between the plasmas and estimate difficult-to-measure parameters of the experiments using standard magnetic field diagnostics. To further understand how the coupling model in Sec. IV can describe the experiments and what improvements must be done for the full application of the model in an experimental context, we now compare it with results from LAPD experiments with laser-driven plasmas and magnetized background plasmas. In particular, we compare the model with runs from LAPD experiments that observed strong coupling between the two plasmas. We note that our model only approximates these systems due to the non-uniform and dynamic (*i.e.* non-steady-state) nature of the laser-driven plasmas in these experiments. Nonetheless, the model provides useful insight into the coupling process and the experiments can help constrain key aspects of the model.

The data chosen for these experiments are shown in Table I. The typical laser-driven plasmas produced in the laboratory are not uniform in density and velocity as our coupling model considers. However, under small scales of the driver expansion and for the strong coupling regimes of the selected runs, some features remain similar to our 1D simulations, such as constant coupling and front velocities, and a plateau region on the magnetic field compression[28,32,33]. In these conditions, we can partially apply the coupling study to experiments.

TABLE I. Coupling parameters of LAPD experiments with laser-driven and magnetized background plasmas[28,32]. We selected runs with $M_A \sim 1$ and strong coupling regimes, *i.e.*, runs with magnetic cavities with approximately no magnetic field inside, a plateau region with a strong magnetic field compression, and constant coupling and front velocities for sufficiently long times. We also selected the run shown in Fig. 2 a) for comparison[33].

Run	v_A (km/s)	v_c (km/s)	v_f (km/s)	α	v_c/v_A	v_f/v_A
Run4 2013[28]	280	164	250	1.6	0.6	0.9
Run3 2015[32]	189	260	440	2.0	1.4	2.3
Mini Mag.[33]	378	135	380	1.3	0.4	1.0

Since the experimental driver is not uniform and we do not always have accurate measurements of the density, length, and velocity of the plasma, we cannot properly calculate the corresponding R_n quantity in these experiments. With Eqs. (13a) to (13c), we obtain $v_f/v_A = \alpha$, and $v_c/v_A = \alpha - 1$. We will use these relations to further evaluate how we can use the coupling model, which considers uniform systems, for the experiments with laser-ablated plasmas and non-uniform conditions.

For the first and second runs in Table I, we have an average compression of $\alpha > 1.5$, leading to strong coupling between the plasmas. For the first run, we observe $v_c/v_A \approx \alpha - 1$, as expected from the coupling model. However, we also observe $v_f/v_A < \alpha$. For the second run, we observe $v_f - v_c \approx v_A$, but also $v_f/v_A > \alpha$. These differences from the coupling model may have emerged from the typical deceleration of the cavity and compression expansions observed in experiments[16,17,28,32], and from the difficulty in measuring precisely some of the coupling parameters from the available data.

In the last row of Table I, we have the coupling parameters for the experiments with ion-scale magnetospheres[33], for the no dipole case, represented in Fig. 2 a). Since $\alpha < 1.5$, this run has weaker coupling between the plasmas than the two previous cases[28,32]. We observe $v_c/v_A \approx \alpha - 1$, but $v_f/v_A < \alpha$. In this run, the plasmas are short and do not interact with each other for enough time to observe a plateau region in the magnetic compression.

As discussed above, the coupling model derived in this paper is unable to fully explain observations in previous experiments (e.g. errors in α vary from $\sim 15-80\%$). From the coupling model, these differences could indicate time varying proprieties and that the coupling does not occur in steady-state. Further effort must be done to fully describe the coupling of the experiments. Other experiments also presented additional differences from the simulations. Some showed velocities for the magnetic cavity and magnetic compression that varied considerably over time[19,20,32] and compressed background regions with a decreasing magnetic field[28]. From the coupling study, these characteristics are mostly likely caused by the expansion of the laser-ablated plasma and the non-uniformity of the densities and velocities, and by having short plasmas, respectively. For further studies of the coupling model, these properties should be considered, as well as high electron and ion temperatures.

The developed coupling model is a stating point to study the coupling for the experiments. However, to some extent, we can still apply it to the experiments. As predicted by the model, decreasing the background density or increasing the driver ion mass should increase v_c and v_f, while increasing the background magnetic field should decrease v_c but increase v_f. This is particular important for ion-scale magnetosphere experiments to insure that the compressed background plasma interacts with the dipole for a sufficient amount of time. This time is dependent on $v_f - v_c$, and too high Mach numbers may not lead to sufficient interaction times. The model also showed that v_c could help estimate the maximum expansion of the cavity, and that the relation between v_c/v_f can help us evaluate the energy transfer between the driver and the background (check Appendix B).

VII. DISCUSSION AND CONCLUSIONS

In recent experiments on the Large Plasma Device (LAPD) at UCLA, ion-scale magnetospheres were performed in the laboratory by driving a laser-produced plasma into a dipolar magnetic field embedded in a uniformly magnetized plasma[33]. Under this configuration, the laser-driven and background plasmas first interact with each other before interacting with the strong magnetic field of the dipole. For the experimental and numerical analysis of laboratory ion-scale magnetospheres, and for the design of future experiments that involve fast plasmas moving toward magnetized plasmas, it is necessary to understand this interaction.

In this paper, we derived analytical expressions for magnetic field parameters that describe the coupling between an unmagnetized driver plasma and a perpendicularly magnetized background plasma. These expressions were then compared with 1D particle-in-cell (PIC) simulations for multiple densities, ion masses, and magnetic field values. For the cold plasmas, and uniform density and velocity profiles considered, the expressions were consistent with simulations. These expressions allow us to (i) evaluate the coupling between the plasmas, (ii) estimate initial quantities from simple magnetic field diagnostics, and (iii) calculate the spatial and temporal scales of these systems.

For the ideal plasmas considered, the simulations reached a near steady-state condition, where the coupling parameters — the average magnetic compression ratio and the velocities of the magnetic cavity and of the magnetic compression — remain constant. These quantities describe the coupling between the plasmas and increase with higher driver-to-background density and ion mass ratios. The compression ratio and the cavity velocity also increase with the Alfvénic Mach number, while the compression velocity decreases. Additionally, for some parameters, the driver plasma does not have enough momentum to push the background forward.

From conservation arguments, we obtained analytical expressions and numerical solutions for the coupling parameters, which were consistent with 1D PIC simulations. Since these parameters can be measured from magnetic field diagnostics, they can be used as a benchmark for the initial conditions of these systems. With these expressions, we can also determine other quantities, such as the stopping distance of the magnetic cavity and the magnetopause position associated with the laboratory ion-scale magnetospheres.

We assumed uniform profiles and long plasmas for the coupling model, and always observed strong coupling and a quasi-steady-state regime in the simulations. In the experiments with laser-driven plasmas and magnetized background plasmas, however, the driver is short, non-uniform, and expanding, and therefore, we do not always observe the same conditions. A complete study of the experimental coupling between the plasmas must consider these characteristics.

In conclusion, we derived analytical expressions for multiple parameters and arbitrary Alfvénic flows that describe the coupling between a driven plasma and a magnetized background plasma. These expressions are consistent with results from PIC simulations and can assist in the design of future experiments with driven plasmas and magnetized obstacles. For future works, we intend to explore other regimes and configurations, such as higher ion and electron temperatures, shorter drivers, and non-uniform densities and velocities.

ACKNOWLEDGMENTS

We acknowledge the support of the European Research Council (InPairs ERC-2015-AdG 695088), FCT (PD/BD/114307/2016, APPLAuSE PD/00505/2012, and UID/FIS/50010/2023), the NSF/DOE Partnership in Basic Plasma Science and Engineering (Award Number PHY-2010248), and PRACE for awarding access to MareNostrum (Barcelona Supercomputing Center, Spain). The simulations presented in this work were performed at the IST cluster (Lisbon, Portugal) and at MareNostrum.

DATA AVAILABILITY STATEMENT

The data that support the findings of this study are openly available in Zenodo at http://doi.org/10.5281/zenodo.7485077, reference number 39.

Appendix A: Electric field of the system

The simulations in this paper considered collisionless and magnetic pressure dominated systems, *i.e.*, $\beta \equiv 8\pi n_e T_e/B^2 \ll 1$, where n_e and T_e are the electron density and temperature, respectively. For low Mach numbers $M_A \sim 1$, neither collisions nor instabilities effectively transfer momentum and energy between the driver and the perpendicularly magnetized background plasma. For these conditions, the laminar electric field provides the dominant coupling mechanism between the two plasmas[28]. Using a hybrid model[24], where the ion species are considered kinetically, and the electron species as a charge-neutralizing fluid, we can describe the electric field of the PIC simulations. Considering that the magnetic field is mostly defined in the z direction, then the laminar collisionless electric field of the system, for the regimes considered, is approximately given by

$$\mathbf{E} \approx -\frac{1}{4\pi e n_e} B_z \nabla_\perp B_z - \frac{1}{e n_e c}(\mathbf{J_d} + \mathbf{J_0}) \times \mathbf{B_z} - \frac{\nabla p}{e n_e} \,. \quad \text{(A1)}$$

In Eq. (A1), $\mathbf{J_j} = Z_j n_j \mathbf{v_j}$ is the current density of the driver ($j = d$) or of the background ($j = 0$) plasmas. Z_j, n_j, and $\mathbf{v_j}$ are the ions' charge, density, and velocity, respectively, for the plasma j. With quasi-neutrality, we have $n_e \approx Z_d n_d + Z_0 n_0$. The first term in Eq. (A1), $\mathbf{E_1} = -B_z \nabla_\perp B_z / 4\pi e n_e$, is primarily defined along the y direction since $|\partial B/\partial x| \ll |\partial B/\partial y|$. The second term, $\mathbf{E_2} = -(\mathbf{J_b} + \mathbf{J_d}) \times \mathbf{B_z}/e n_e c$, however, is mostly defined in x, with $\mathbf{E_2} \approx -(v_y/c) B_z \,\mathbf{x}$, since the ion motions are mostly defined along y. The third term $\mathbf{E_3} = -\nabla p / e n_e$ is associated with the electron pressure p.

To verify if Eq. (A1) correctly describes the electric field of the system, the terms in Eq. (A1) and the electric field of the simulation with $n_d/n_0 = 2$, $m_{i,d}/m_{i,0} = 1$, and $M_A = 1.5$ (previously presented in Fig. 5), are compared in Fig. 13, for $t\omega_{ci} \approx 5.0$.

Figures/laminar-electric-field.pdf

FIG. 13. Comparison between the terms of Eq. (A1) and the electric field of the simulation with $n_d/n_0 = 2$, $m_{i,d}/m_{i,0} = 1$, and $M_A = 1.5$, for $t\omega_{ci} \approx 5.0$. The y components of the electric field are shown in a) and the x components in b). E_y and E_x refer to the electric field profiles of the simulation (blue), and E_1 and E_2 to the first and second terms of Eq. (A1) (orange). Both frames also show the magnetic field B_z (green). [Associated dataset available at https://zenodo.org/record/7485077 (Ref. 39).]

Fig. 13 shows that we can use Eq. (A1) to calculate the electric field of these systems. In Fig. 13 a), we see that the y component of the electric field can be expressed by $\mathbf{E_1}$, which depends on the magnetic field gradient. Within the interface that separates the magnetic cavity from the compressed magnetic field, we observe a significant negative electric field.

AIP Publishing

Physics of Plasmas ACCEPTED MANUSCRIPT

This is the author's peer reviewed, accepted manuscript. However, the online version of record will be different from this version once it has been copyedited and typeset.

PLEASE CITE THIS ARTICLE AS DOI: 10.1063/5.0144725

This electric field is responsible for the reflection of the driver ions back to the upstream region.

Fig. 13 b) also shows that the x component of the electric field can be described by $\mathbf{E_2}$. In the background region, E_x is always negative and approximately $-(v_y/c)B_z$, in agreement with Ohm's law, $\mathbf{E}+\mathbf{v}\times\mathbf{B}/c=0$. For the low Mach numbers and low β considered, $\mathbf{E_3}$ is typically negligible when compared to the electric field terms $\mathbf{E_1}$ and $\mathbf{E_2}$.

We can use Eq. (A1) to describe the motion of the particles, in particular, the reflection of the driver particles by the background plasma region. Near this region, unmagnetized driver ions move with velocity v_0 against the compressed background magnetic field of average value αB_0. The discontinuity region (labeled as A in Fig. 7) moves with velocity v_c, and the driver ions end up reflected upstream with velocity v_1. From Eq. (A1), this field is approximately given by

$$E_y \approx -\frac{1}{4\pi e n_e} B_z \frac{\partial B_z}{\partial y} - \frac{1}{e n_e}\frac{\partial p}{\partial y}\ . \tag{A2}$$

Since $|E_y| \gg |v_x B_z/c|$ for this region, the equation of motion for a reflecting driver ion is

$$m_{i,d}\frac{dv'_{i,d,y}}{dt'} = m_{i,d}\frac{dv'_{i,d,y}}{dy'}v'_{i,d,y} = Z_d e E_y\ , \tag{A3}$$

where $v'_{i,d,y} \equiv v_{i,d,y} - v_c$ is the driver ion velocity in the reference frame of the discontinuity. In this frame, the driver ions have initial velocity $v'_{i,d,y} = v_0 - v_c$ and start to be reflected upstream when $v'_{i,d,y} = 0$. By integrating Eq. (A3), and considering p_2 as the average electron pressure of the compressed background plasma, we obtain

$$\begin{aligned}\int_{v_0-v_c}^{0} v'_{i,d,y}\, dv'_{i,d,y} = &-\frac{Z_d}{4\pi m_{i,d}}\int_0^{\alpha B_0}\frac{B'_z}{n'_e}dB'_z \\ &-\frac{Z_d}{m_{i,d}}\int_0^{p_2}\frac{1}{n'_e}dp'\ .\end{aligned} \tag{A4}$$

We consistently observed a peak in the electron density of $n_e \approx 4\ Z_d n_d$ in the interface driver-background of the simulations. Assuming this value in Eq. (A4), we end up with

$$\begin{aligned}\frac{(v_0-v_c)^2}{2} &= \frac{1}{4\pi m_{i,d}}\frac{(\alpha B_0)^2}{8n_d} + \frac{1}{m_{i,d}}\frac{p_2}{4n_d} \\ \Longrightarrow 2n_d m_{i,d}(v_0-v_c)^2 &= p_2 + \frac{(\alpha B_0)^2}{8\pi}\ ,\end{aligned} \tag{A5}$$

which corresponds to the pressure balance of Eq. (6) for $\beta_d \ll 1$, as expected.

Appendix B: Energy expressions

To validate the assumption $\alpha \approx M_B \equiv v_f/v_A$ for low Mach numbers considered in Sec. IV C, we now compare the different energy fluxes terms represented in Eq. (2d) with the total energies measured in multiple simulations. Considering ϕ_{d}, ϕ_0, ϕ_{mag}, and ϕ_{ele} the energy fluxes of the system associated with the driver plasma, background plasma, magnetic field, and electric field, respectively, in the lab frame, over a time δt and transverse area a_t, we must have, due to energy conservation

$$\Phi_{\mathrm{d}} + \Phi_0 + \Phi_{\mathrm{mag}} + \Phi_{\mathrm{ele}} = 0\ . \tag{B1}$$

Since $|\Phi_{\mathrm{ele}}/\Phi_{\mathrm{mag}}| \sim (v_0/c)^2 \ll 1$ (see Appendix A), Φ_{ele} can be neglected in Eq. (B1).

In Fig. 7, we observe that the driver consists of two populations, with velocity v_0 and v_1. The energy flux of each population can be calculated by multiplying the kinetic energy of each ion with the rate of the number of ions. Recalling from Sec. IV B that $n'_d = n_d$ and $v_1 = 2v_c - v_0$, the interface driver-background travels with velocity v_c, and assuming cold plasmas ($\beta_1, \beta_d \ll 1$), we obtain that the driver energy flux in the lab frame can be calculated with

$$\begin{aligned}\Phi_{\mathrm{d}} &= -\frac{1}{2}m_{i,d}v_0^2 n_d(v_0-v_c) + \frac{1}{2}m_{i,d}v_1^2 n'_d(v_c-v_1) \\ &= -2n_d m_{i,d}(v_0-v_c)^2 v_c\ .\end{aligned} \tag{B2}$$

Unlike the driver, the background plasma is located in two different regions in Fig. 7. In the magnetic compression region, the average kinetic energy flow of each background ion is $m_{i,0}v_c^2/2$, and the density is $n'_0 = \alpha n_0$. In the unperturbed background region, the background plasma has no flow velocity. For low Mach numbers and cold plasmas, we can ignore the contribution of the compressed background electron pressure p_2. Since the back and front boundaries of the compression region travel with velocities v_c and v_f, respectively, we can then express the background energy flux associated with the plasmas flow as

$$\Phi_0 = \frac{1}{2}m_{i,0}v_c^2 n'_0(v_f - v_c) = \frac{1}{2}m_{i,0}v_c^3 n_0\frac{\alpha}{\alpha-1}\ . \tag{B3}$$

Finally, we need an expression for the magnetic energy flux. The magnetic compression region has an average magnetic field of αB_0 and increases its length at a velocity $v_f - v_c$, while the unperturbed background region has a magnetic field B_0 and a length that decreases at a velocity $-v_f$. The magnetic energy flux is thus

$$\Phi_{\mathrm{mag}} = \frac{(\alpha B_0)^2}{8\pi}(v_f - v_c) - \frac{B_0^2}{8\pi}v_f = \frac{B_0^2}{8\pi}\alpha v_c\ . \tag{B4}$$

To validate the previous expressions for the energy fluxes, we performed multiple simulations with different Alfvénic Mach numbers M_A and driver-to-background density ratios n_d/n_0, with $m_{i,d}/m_{i,0} = 1$. For each simulation, we measured the coupling parameters α and v_c from the magnetic field data, and then, with these values, we calculated the theoretical energy fluxes with Eqs. (B2) to (B4).

In Fig. 14, the calculated energy fluxes of a) the driver plasma Φ_{d} and b) the magnetic field Φ_{mag} are compared to the correspondent energy fluxes obtained from the variation of the total energies in the simulations. Each quantity was measured in the quasi-steady-state regime of the simulations.

Fig. 14 confirms that Eqs. (B2) and (B4) can be used to describe the driver and magnetic energy fluxes of the system, `Figures/MA-nd-energy-drbg-scan.pdf`

FIG. 14. Energy fluxes of a) the driver ions Φ_d and b) the magnetic field Φ_mag, for multiple simulations with different Alfvénic Mach numbers M_A and density ratios n_d/n_0. We considered $m_{i,d}/m_{i,0} = 1$. The energy fluxes calculated from the total energy are represented by scatter points, while the energy fluxes calculated with Eqs. (B2) and (B4), and with the measured α and v_c values, are connected by dashed lines. [Associated dataset available at https://zenodo.org/record/7485077 (Ref. 39).]

`Figures/MA-nd-energy-bgth-scan.pdf`

FIG. 15. a) Energy flux of the background plasma Φ_0, for multiple simulations with different Alfvénic Mach numbers M_A and density ratios n_d/n_0. We considered $m_{i,d}/m_{i,0} = 1$. The fluxes calculated from the total energy are represented by scatter points, while the energy fluxes calculated from Eq. (B3), and with the measured α and v_c values, are connected by dashed lines. b) Fraction of thermal energy to total energy of the background ions, in the final stage of the main interaction, for each simulation. [Associated dataset available at https://zenodo.org/record/7485077 (Ref. 39).]

for the regimes considered. In Fig. 14 a) we observe that the flux of energy lost by the driver increases for higher driver densities and lower Mach numbers, leading to a more efficient energy transfer from the driver to the background. Similarly, in Fig. 14 b), the magnetic energy flux is larger for denser drivers and lower Mach numbers.

In Fig. 14, we also observe that in the simulation with $M_A = 0.5$ and $n_d/n_0 = 0.5$, it is the magnetic field that transfers energy to the driver plasma. This simulation corresponds approximately to the case where the initial magnetic pressure $B_0^2/8\pi$ is larger than the driver's ram pressure $2n_d m_{i,d} v_0^2$ (*i.e.*, $R_n > M_A$), and so, the driver is pushed back by the background, leading to a negative coupling velocity.

Fig. 15 a) compares the background energy flux Φ_0 calculated with Eq. (B3) with the energy flux obtained from the total energy of the simulations. As we can see, Eq. (B3) is more consistent with the simulations for low Mach numbers, than for high Mach numbers and driver densities.

For high Mach numbers, instabilities start to form in the background plasma. This leads to an increase in the thermal energy of the plasma, which starts to have an important role in the energy partition of the system. Since Eq. (B3) neglects instabilities and thermal effects, it underestimates the energy flux of the background plasma, as we observe in Fig. 15 a). Fig. 15 b) shows the average ratio of thermal energy of the background ions $E_{i,0,th}$ to their total energy $E_{i,0,tot}$, near the final stage of the main interaction in the simulations. As expected, we observe that, for high Mach numbers and driver densities, a significant percentage of the background ions' energy is thermal energy, while for low Mach numbers, the thermal energy is negligible.

The thermal effects of the ions in the compressed background can be estimated with the pressure p_2. If we assume Eqs. (13a) and (13c) for α and v_f, respectively, and apply Eq. (10), we obtain that the ratio of the plasma pressure to magnetic pressure in the compressed background region is given by

$$\frac{8\pi p_2}{(\alpha B_0)^2} = \frac{\beta_2}{\alpha^2} \approx \left(\frac{\alpha-1}{\alpha}\right)^2 = \left(\frac{v_c}{v_f}\right)^2 . \tag{B5}$$

As we can see in Fig. 8, the coupling velocity v_c increases with the Mach number M_A and the density ratio n_d/n_0, while the front velocity v_f decreases with M_A but increases with n_d/n_0. As a result, the ratio in Eq. (B5) decreases for low Mach numbers. In this regime, we can then ignore the p_2 term in the energy conservation.

By applying Eqs. (B2) through (B4) in Eq. (B1), it is possible to show that $\alpha \approx v_f/v_A = M_B$ for low Mach numbers. Additionally, we obtain from Eq. (12) for $\gamma = 2$ and $\beta_1 \ll 1$ that $\alpha = M_B$ for $M_B = 0$, 1, and $\gamma/(\gamma-1) = 2$. As a result, we observe that Eq. (12) follows $\alpha \approx M_B$ for low Mach numbers $M_B < 2$.

From Eqs. (B2) and (B3), we also obtain that the ratio of energy transferred from the driver plasma to the background plasma is

$$-\frac{\Phi_0}{\Phi_\mathrm{d}} = \frac{M_A - R_n}{M_A + 1} = \frac{v_c}{v_f} \ . \tag{B6}$$

The ratio between the velocities of the magnetic cavity and of the magnetic compression is then a direct tool to evaluate the efficiency of the energy transfer from the driver to the background plasmas.

[1] L. F. Burlaga, R. M. Skoug, C. W. Smith, D. F. Webb, T. H. Zurbuchen, and A. Reinard, "Fast ejecta during the ascending phase of solar cycle 23: ACE observations, 1998-1999," Journal of Geophysical Research: Space Physics **106**, 20957–20977 (2001).

[2] D. S. Spicer, R. W. Clark, S. P. Maran, and R. W. Clark, "A Model of the Pre-Sedov Expansion Phase of Supernova Remnant-Ambient Plasma Coupling and X-Ray Emission from SN 1987A," Astrophysical Journal; (USA) **356**, 549 (1990).

[3] D. Mendis and W.-H. Ip, "The ionospheres and plasma tails of comets," Space Science Reviews **20**, 145–190 (1977).

[4] S. M. Krimigis, G. Haerendel, R. W. McEntire, G. Paschmann, and D. A. Bryant, "The active magnetospheric particle tracer explorers (AMPTE) program," Eos, Transactions American Geophysical Union **63**, 843–850 (1982).

[5] M. H. Johnson and J. Kierein, "Combined release and radiation effects satellite (crres): Spacecraft and mission," Journal of Spacecraft and Rockets **29**, 556–563 (1992).

[6] P. Dyal, "Particle and field measurements of the starfish diamagnetic cavity," Journal of Geophysical Research: Space Physics **111** (2006), https://doi.org/10.1029/2006JA011827.

[7] D. W. Hewett, S. H. Brecht, and D. J. Larson, "The physics of ion decoupling in magnetized plasma expansions," Journal of Geophysical Research: Space Physics **116** (2011), https://doi.org/10.1029/2011JA016904.

[8] D. Winske and S. P. Gary, "Hybrid simulations of debris-ambient ion interactions in astrophysical explosions," Journal of Geophysical Research: Space Physics **112** (2007), https://doi.org/10.1029/2007JA012276.

[9] D. A. Gurnett, R. R. Anderson, T. Z. Ma, G. Haerendel, G. Paschmann, O. H. Bauer, R. A. Treumann, H. C. Koons, R. H. Holzworth, and H. Lühr, "Waves and electric fields associated with the first ampte artificial comet," Journal of Geophysical Research: Space Physics **91**, 10013–10028 (1986).

[10] W. H. Ip and W. I. Axford, "The formation of a magnetic-field-free cavity at comet Halley," (1987).

[11] P. A. Bernhardt, "Probing the magnetosphere using chemical releases from the combined release and radiation effects satellite," Physics of Fluids B: Plasma Physics **4**, 2249–2256 (1992).

[12] Y. Zakharov, M. Alexandr, P. Amold, and P. Vitali, "Diamagnetic cavity of plasma clouds expanding in magnetized media," Journal of Plasma and Fusion Research **2**, 398 (1999).

[13] A. Collette and W. Gekelman, "Structure of an exploding laser-produced plasma," Phys. Rev. Lett. **105**, 195003 (2010).

[14] Goetz, C., Koenders, C., Richter, I., Altwegg, K., Burch, J., Carr, C., Cupido, E., Eriksson, A., Güttler, C., Henri, P., Mokashi, P., Nemeth, Z., Nilsson, H., Rubin, M., Sierks, H., Tsurutani, B., Vallat, C., Volwerk, M., and Glassmeier, K.-H., "First detection of a diamagnetic cavity at comet 67p/churyumov-gerasimenko," A&A **588**, A24 (2016).

[15] D. B. Schaeffer, L. R. Hofer, E. N. Knall, P. V. Heuer, C. G. Constantin, and C. Niemann, "A platform for high-repetition-rate laser experiments on the large plasma device," High Power Laser Science and Engineering **6**, e17 (2018).

[16] D. Winske, J. D. Huba, C. Niemann, and A. Le, "Recalling and updating research on diamagnetic cavities: Experiments, theory, simulations," Frontiers in Astronomy and Space Sciences **5** (2019), 10.3389/fspas.2018.00051.

[17] B. H. Ripin, J. D. Huba, E. A. McLean, C. K. Manka, T. Peyser, H. R. Burris, and J. Grun, "Sub-alfvénic plasma expansion," Physics of Fluids B: Plasma Physics **5**, 3491–3506 (1993).

[18] M. VanZeeland and W. Gekelman, "Laser-plasma diamagnetism in the presence of an ambient magnetized plasma," Physics of Plasmas **11**, 320–323 (2004).

[19] J. Bonde, "Collisionless coupling of a high-β expansion to an ambient, magnetized plasma. i. rayleigh model and scaling," Physics of Plasmas **25**, 042109 (2018).

[20] J. Bonde, S. Vincena, and W. Gekelman, "Collisionless coupling of a high-β expansion to an ambient, magnetized plasma. ii. experimental fields and measured momentum coupling," Physics of Plasmas **25**, 042110 (2018).

[21] A. Le, D. Winske, A. Stanier, W. Daughton, M. Cowee, B. Wetherton, and F. Guo, "Astrophysical explosions revisited: Collisionless coupling of debris to magnetized plasma," Journal of Geophysical Research: Space Physics **126**, e2021JA029125 (2021).

[22] N. Behera, A. Kumar, and R. K. Singh, "Cavitation and charge separation in laser-produced copper and carbon plasma in transverse magnetic field," Plasma Research Express **3**, 025011 (2021).

[23] S. E. Clark, E. T. Everson, D. B. Schaeffer, A. S. Bondarenko, C. G. Constantin, C. Niemann, and D. Winske, "Enhanced collisionless shock formation in a magnetized plasma containing a density gradient," Phys. Rev. E **90**, 041101 (2014).

[24] A. S. Bondarenko, D. B. Schaeffer, E. T. Everson, S. E. Clark, B. R. Lee, C. G. Constantin, S. Vincena, B. Van Compernolle, S. K. Tripathi, D. Winske, and C. Niemann, "Collisionless momentum transfer in space and astrophysical explosions," Nature Physics **13**, 573–576 (2017).

[25] R. W. Clark, J. Denavit, and K. Papadopoulos, "Laminar interactions in high Mach number plasma flows," The Physics of Fluids **16**, 1097–1101 (1973).

[26] I. H. Cairns and C. L. Grabbe, "Towards an mhd theory for the standoff distance of earth's bow shock," Geophysical Research Letters **21**, 2781–2784 (1994).

[27] S. E. Clark, D. Winske, D. B. Schaeffer, E. T. Everson, A. S. Bondarenko, C. G. Constantin, and C. Niemann, "Hybrid simulation of shock formation for super-alfvénic expansion of laser ablated debris through an ambient, magnetized plasma," Physics of Plasmas **20**, 082129 (2013).

[28] E. T. Everson, *Magnetic Field Characterization of a Diamagnetic Cavity Piston for Generation of Quasi-Perpendicular Collisionless Shocks*, Ph.D. thesis, University of California, Los Angeles (2016).

[29] R. P. Drake, "The design of laboratory experiments to produce collisionless shocks of cosmic relevance," Physics of Plasmas **7**, 4690–4698 (2000).

[30] C. Niemann, W. Gekelman, C. G. Constantin, E. T. Everson, D. B. Schaeffer, A. S. Bondarenko, S. E. Clark, D. Winske, S. Vincena, B. Van Compernolle, and P. Pribyl, "Observation of collisionless shocks in a large current-free laboratory plasma," Geophysical Research Letters **41**, 7413–7418 (2014).

[31] C. Niemann, W. Gekelman, C. G. Constantin, E. T. Everson, D. B. Schaeffer, S. E. Clark, D. Winske, A. B. Zylstra, P. Pribyl, S. K. P. Tripathi, D. Larson, S. H. Glenzer, and A. S. Bondarenko, "Dynamics of exploding plasmas in a large magnetized plasma," Physics of Plasmas **20**, 012108 (2013).

[32] D. B. Schaeffer, E. T. Everson, A. S. Bondarenko, S. E. Clark, C. G. Constantin, D. Winske, W. Gekelman, and C. Niemann, "Experimental study of subcritical laboratory magnetized collisionless shocks using a laser-driven magnetic piston," Physics of Plasmas **22**, 113101 (2015).

[33] D. B. Schaeffer, F. D. Cruz, R. S. Dorst, F. Cruz, P. V. Heuer, C. G. Constantin, P. Pribyl, C. Niemann, L. O. Silva, and A. Bhattacharjee, "Laser-driven, ion-scale magnetospheres in laboratory plasmas. i. experimental platform and first results," Physics of Plasmas **29**, 042901 (2022).

[34] W. Gekelman, H. Pfister, Z. Lucky, J. Bamber, D. Leneman, and J. Maggs, "Design, construction, and properties of the large plasma research device-the lapd at ucla," Review of Scientific Instruments **62**, 2875–2883 (1991).

[35] F. D. Cruz, D. B. Schaeffer, F. Cruz, and L. O. Silva, "Laser-driven, ion-scale magnetospheres in laboratory plasmas. ii. particle-in-cell simulations," Physics of Plasmas **29**, 032902 (2022).

[36] R. A. Fonseca, L. O. Silva, F. S. Tsung, V. K. Decyk, W. Lu, C. Ren, W. B. Mori, S. Deng, S. Lee, T. Katsouleas, and J. C. Adam, "OSIRIS: A three-dimensional, fully relativistic particle in cell code for modeling plasma based accelerators," in *Lecture Notes in Computer Science (including subseries Lecture Notes in Artificial Intelligence and Lecture Notes in Bioinformatics)*, Vol. 2331 LNCS (Springer Verlag, 2002) pp. 342–351.

[37] R. A. Fonseca, J. Vieira, F. Fiuza, A. Davidson, F. S. Tsung, W. B. Mori, and L. O. Silva, "Exploiting multi-scale parallelism for large scale numerical modelling of laser wakefield accelerators," Plasma Physics and Controlled Fusion **55** (2013), 10.1088/0741-3335/55/12/124011.

AIP Publishing Physics of Plasmas ACCEPTED MANUSCRIPT

This is the author's peer reviewed, accepted manuscript. However, the online version of record will be different from this version once it has been copyedited and typeset.

PLEASE CITE THIS ARTICLE AS DOI: 10.1063/5.0144725

[38] Y. Zakharov, "Collisionless laboratory astrophysics with lasers," IEEE Transactions on Plasma Science **31**, 1243–1251 (2003).

[39] F. D. Cruz, D. B. Schaeffer, F. Cruz, and L. O. Silva, "Strong collisionless coupling between an unmagnetized driver plasma and a magnetized background plasma," (2023), https://doi.org/10.5281/zenodo.7485077.

[40] T. Takezaki, K. Takahashi, T. Sasaki, T. Kikuchi, and N. Harada, "Accelerated ions from pulsed-power-driven fast plasma flow in perpendicular magnetic field," Physics of Plasmas **23**, 062904 (2016).

[41] T. Takezaki, S. Kato, T. Oguchi, S. Watanabe, K. Takahashi, T. Sasaki, T. Kikuchi, and H. Ito, "Effect of multi-ion species on collisionless plasma driven by a compact plasma focus device in perpendicular magnetic field," Physics of Plasmas **28**, 102109 (2021).

[42] D. Oliveira, "Magnetohydrodynamic shocks in the interplanetary space: A theoretical review," Brazilian Journal of Physics **47**, 81–95 (2017).

[43] M. G. Kivelson and M. G. Kivelson, *Introduction to space physics* (Cambridge university press, 1995).

[44] A. Balogh and R. A. Treumann, *Physics of collisionless shocks: space plasma shock waves* (Springer Science & Business Media, 2013).

[45] W. B. Thompson, *An introduction to plasma physics* (Elsevier, 2013).

[46] J. Vink, *Physics and Evolution of Supernova Remnants* (Springer, 2020).

[47] D. B. Schaeffer, A. S. Bondarenko, E. T. Everson, S. E. Clark, C. G. Constantin, and C. Niemann, "Characterization of laser-produced carbon plasmas relevant to laboratory astrophysics," Journal of Applied Physics **120**, 043301 (2016).

[48] M. I. Pudovkin, C.-V. Meister, B. P. Besser, and H. K. Biernat, "The effective polytropic index in a magnetized plasma," Journal of Geophysical Research: Space Physics **102**, 27145–27149 (1997).

[49] M. Pudovkin, C.-V. Meister, and B. Besser, "Adiabatic indices in a convecting anisotropic plasma," Astronomische Nachrichten **320**, 87–93 (1999).

[50] J. Y. Kim, G. Go, Y. S. Hwang, and K.-J. Chung, "Dependence of the polytropic index of plasma on magnetic field," New Journal of Physics **23**, 052001 (2021).

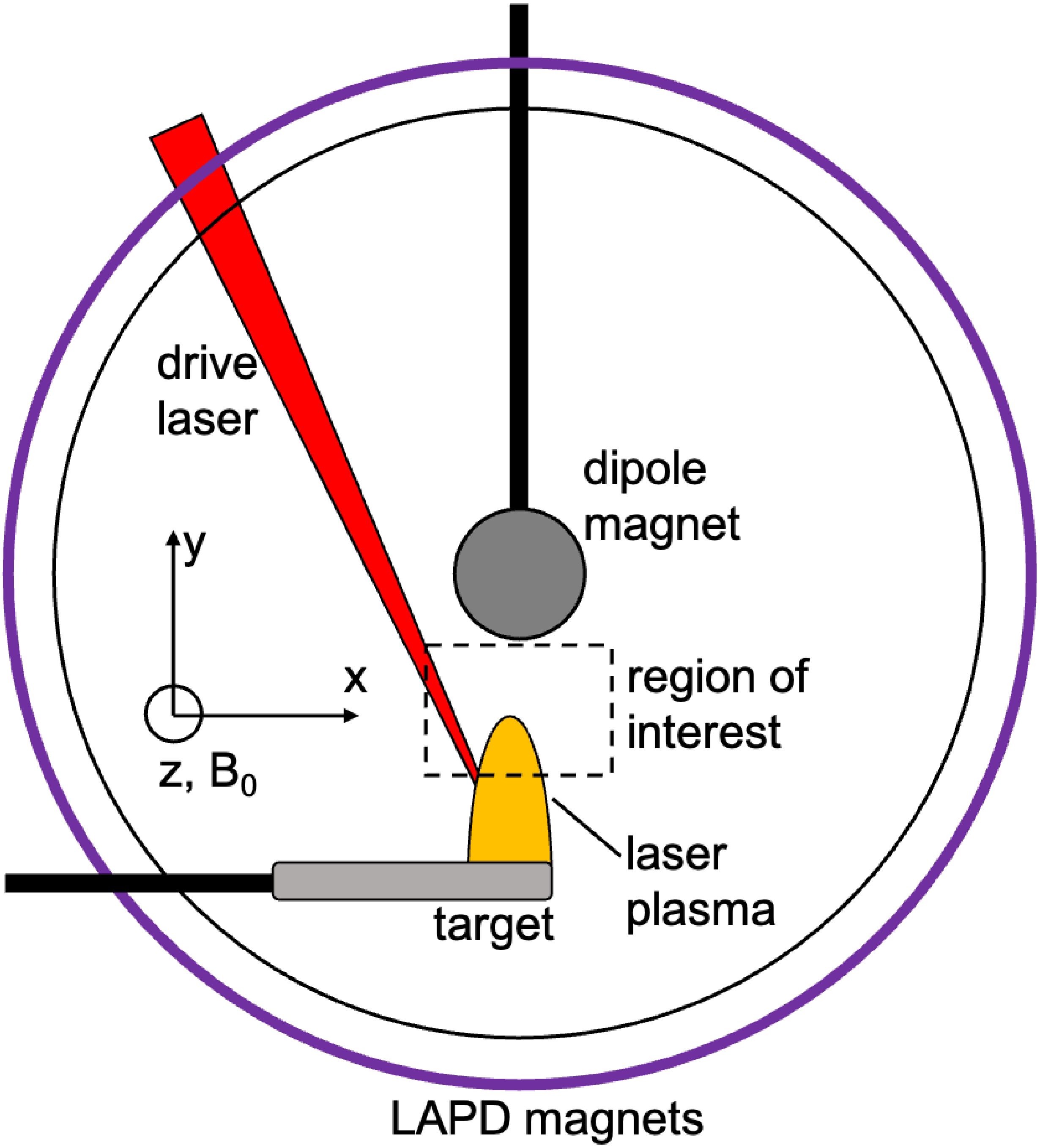
drive laser
dipole magnet
y
x
z, B_0
region of interest
laser plasma
target
LAPD magnets

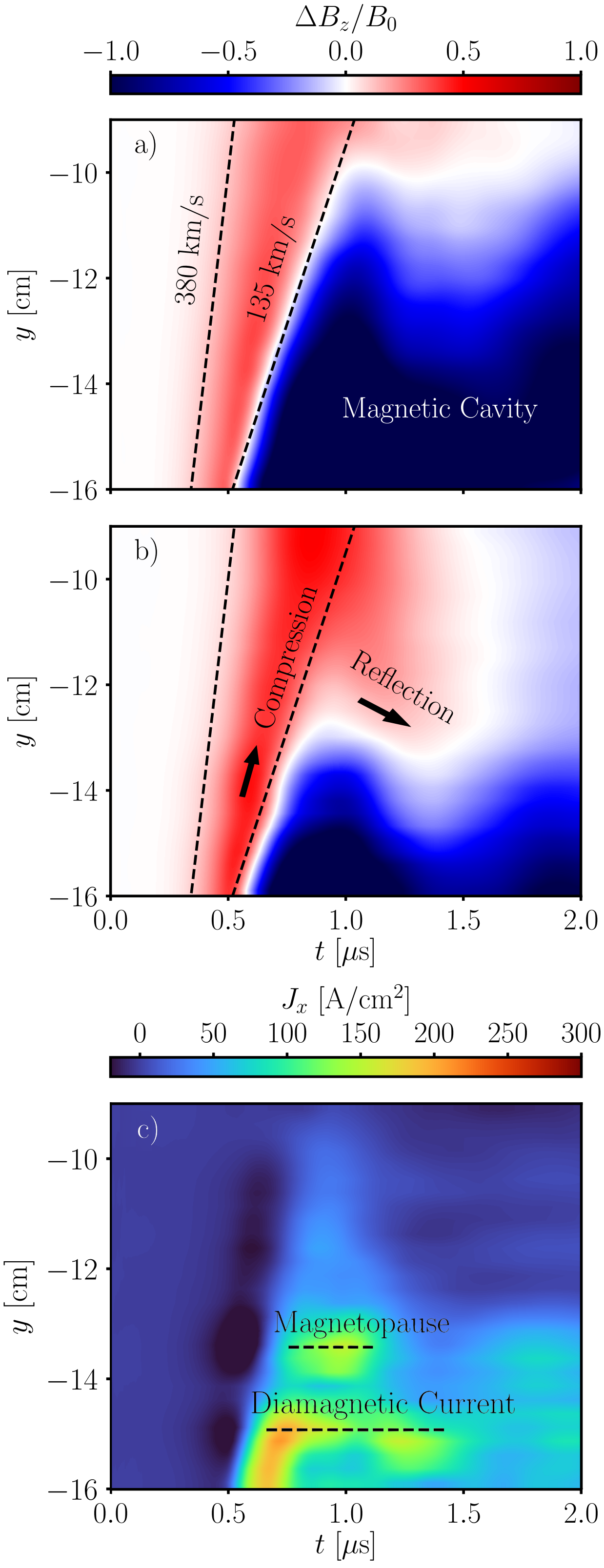
$\Delta B_z/B_0$
−1.0
−0.5
0.0
0.5
1.0
a)
380 km/s
135 km/s
Magnetic Cavity
y [cm]
−10
−12
−14
−16
b)
Compression
Reflection
0.0
0.5
1.0
1.5
2.0
t [μs]
J_x [A/cm^2]
0
50
100
150
200
250
300
c)
Magnetopause
Diamagnetic Current

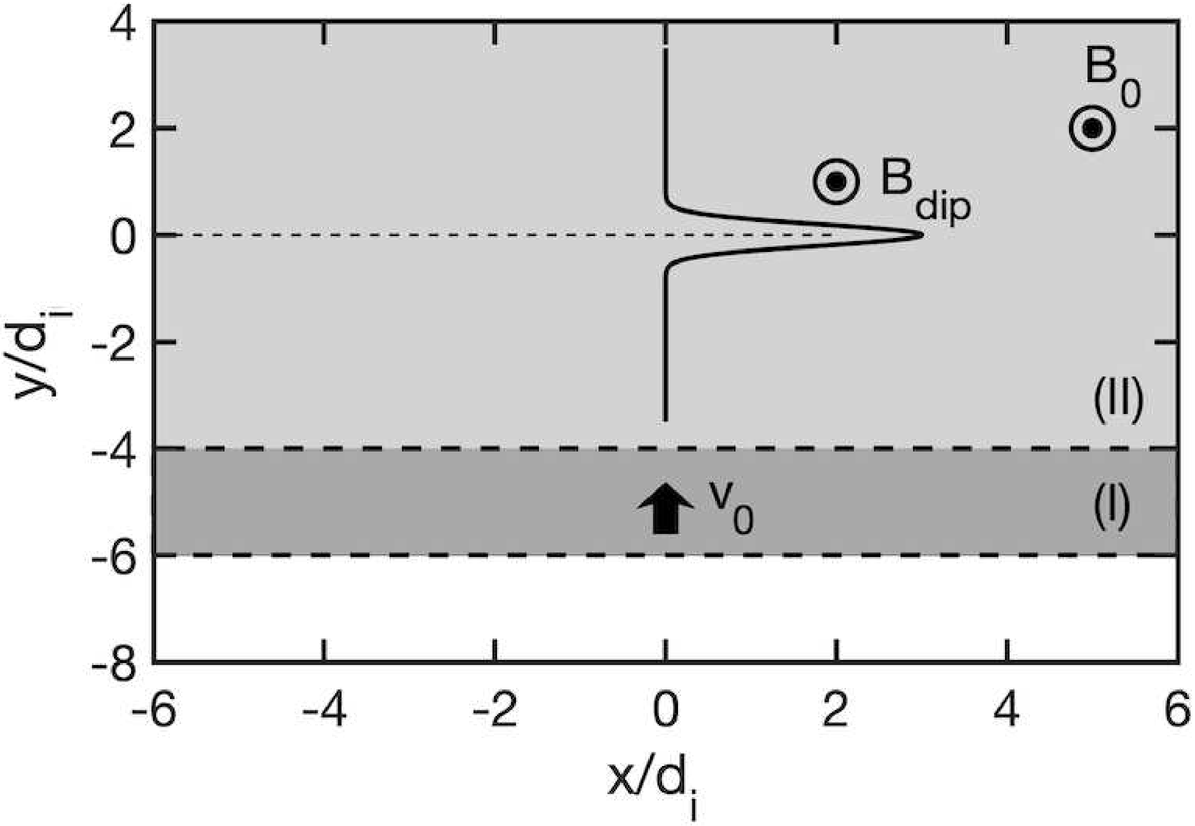
B_0
B_{dip}
v_0
(II)
(I)
y/d$_i$
x/d$_i$
4
2
0
-2
-4
-6
-8
-6
-4
-2
0
2
4
6

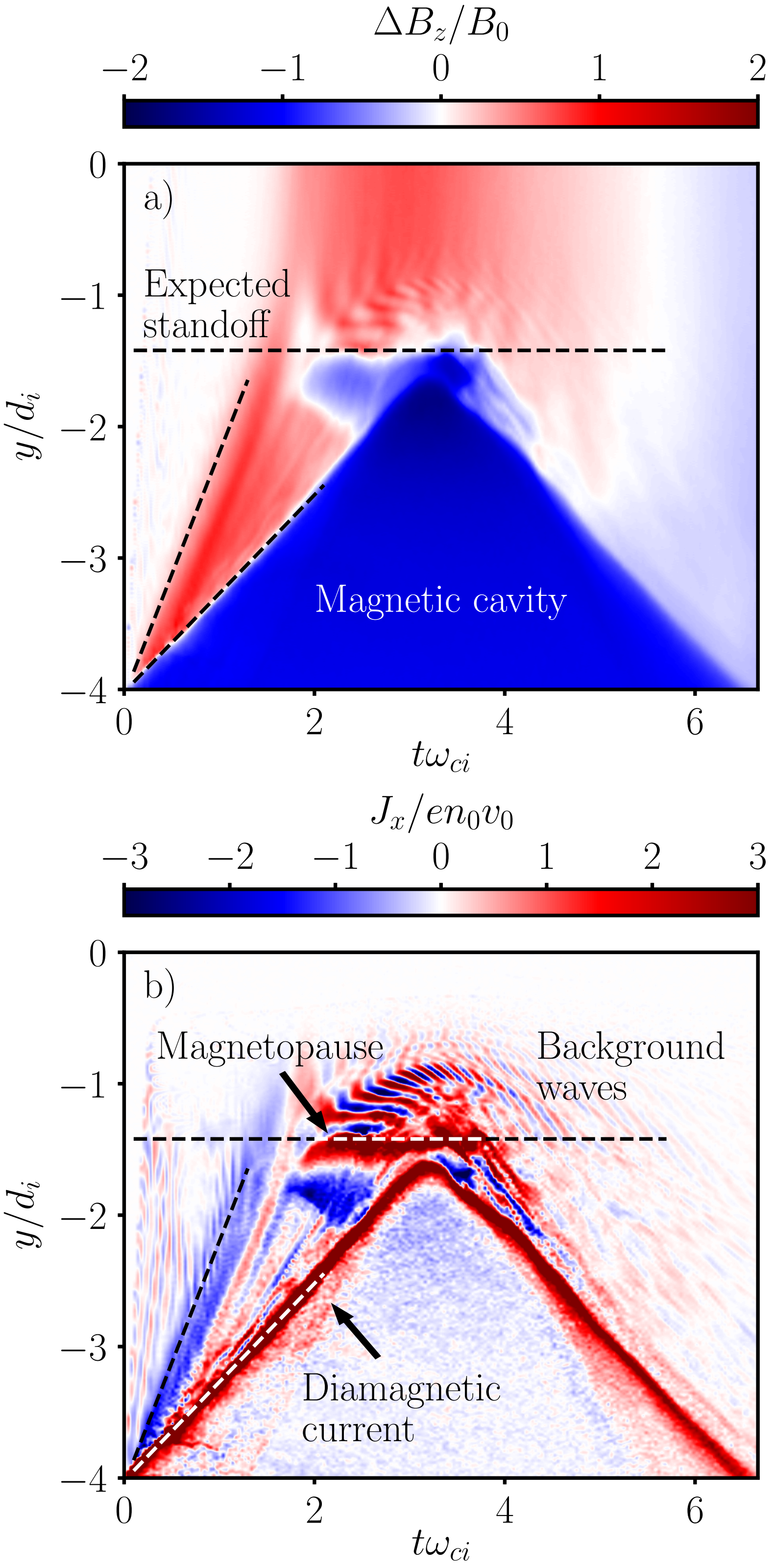
$\Delta B_z/B_0$
−2
−1
0
1
2
a)
Expected standoff
Magnetic cavity
0
−1
−2
−3
−4
y/d_i
0
2
4
6
$t\omega_{ci}$
J_x/en_0v_0
−3
−2
−1
0
1
2
3
b)
Magnetopause
Background waves
Diamagnetic current
0
−1
−2
−3
−4
y/d_i
0
2
4
6
$t\omega_{ci}$

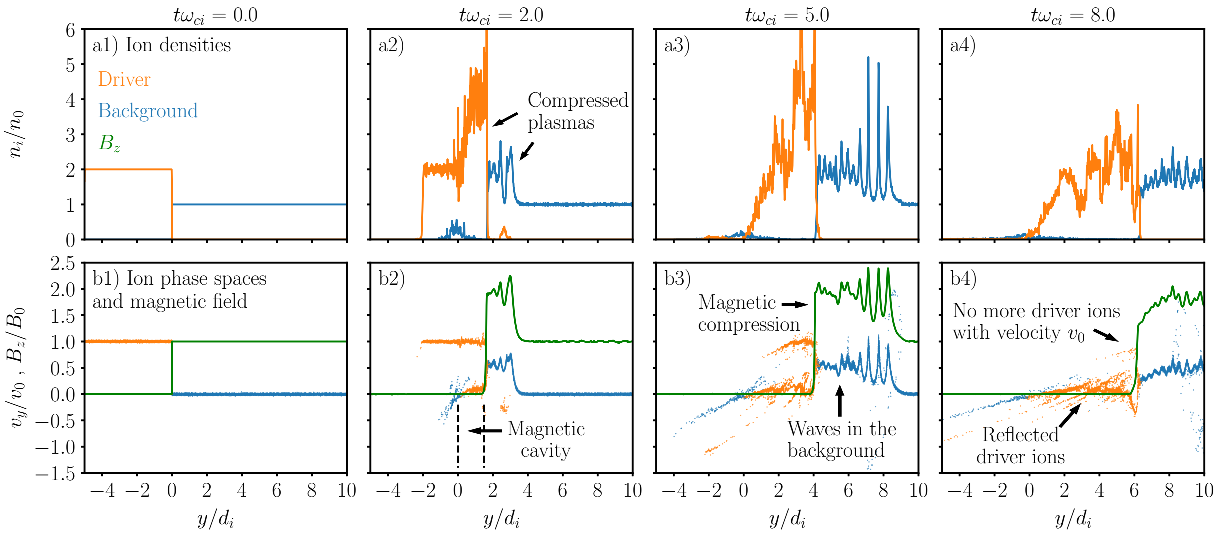
$t\omega_{ci} = 0.0$
$t\omega_{ci} = 2.0$
$t\omega_{ci} = 5.0$
$t\omega_{ci} = 8.0$
a1) Ion densities
Driver
Background
B_z
a2)
Compressed plasmas
a3)
a4)
n_i/n_0
b1) Ion phase spaces and magnetic field
b2)
Magnetic cavity
b3)
Magnetic compression
Waves in the background
b4)
No more driver ions with velocity v_0
Reflected driver ions
v_y/v_0 , B_z/B_0
y/d_i
0
1
2
3
4
5
6
−1.5
−1.0
−0.5
0.0
0.5
1.0
1.5
2.0
2.5
−4
−2
0
2
4
6
8
10

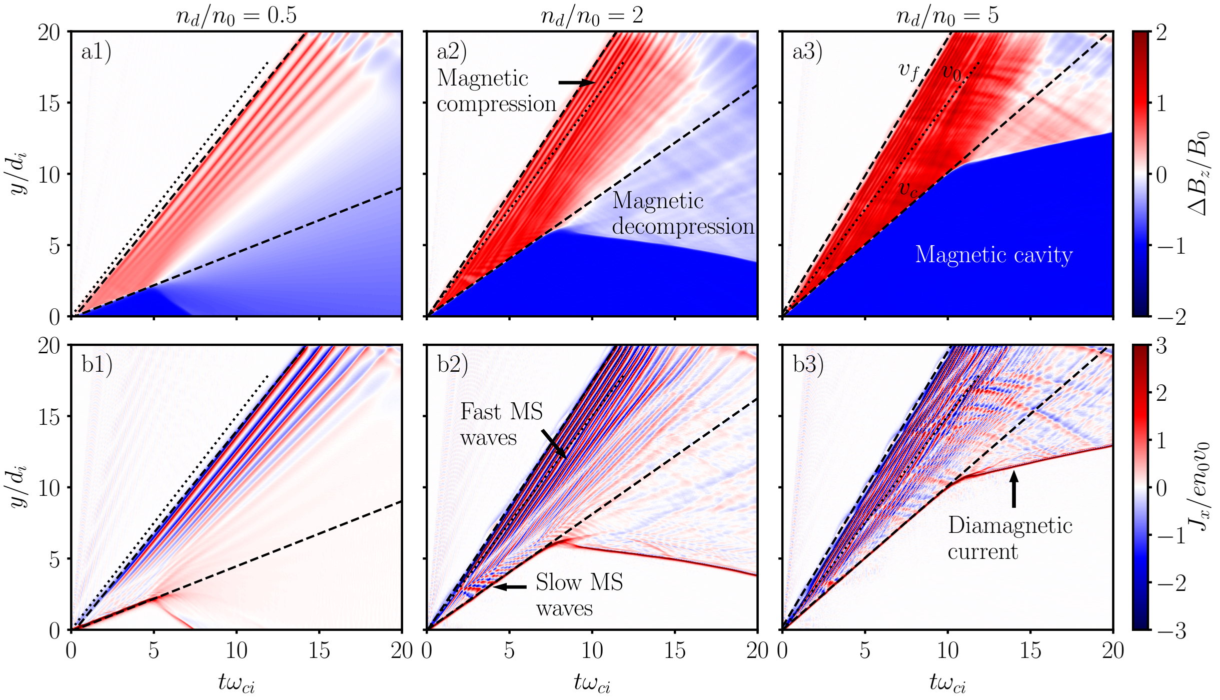
$n_d/n_0 = 0.5$
$n_d/n_0 = 2$
$n_d/n_0 = 5$
a1)
a2)
a3)
b1)
b2)
b3)
Magnetic compression
Magnetic decompression
Magnetic cavity
v_f
v_0
v_c
Fast MS waves
Slow MS waves
Diamagnetic current
y/d_i
$t\omega_{ci}$
$\Delta B_z/B_0$
J_x/en_0v_0
0
5
10
15
20
−2
−1
0
1
2
−3
−2
−1
0
1
2
3

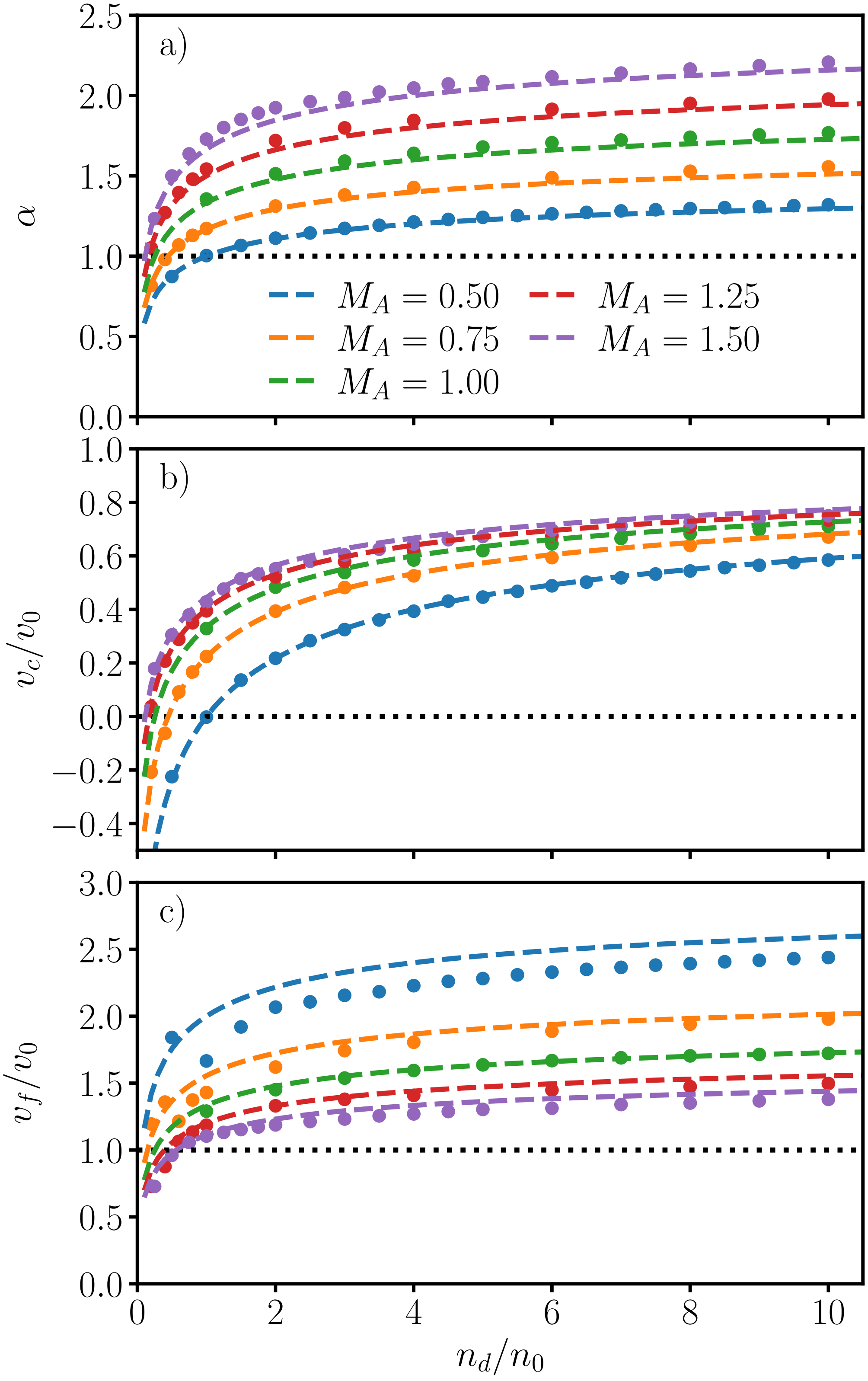
a)
α
2.5
2.0
1.5
1.0
0.5
0.0
$M_A = 0.50$
$M_A = 0.75$
$M_A = 1.00$
$M_A = 1.25$
$M_A = 1.50$
b)
v_c/v_0
1.0
0.8
0.6
0.4
0.2
0.0
−0.2
−0.4
c)
v_f/v_0
3.0
2.5
2.0
1.5
1.0
0.5
0.0
0
2
4
6
8
10
n_d/n_0

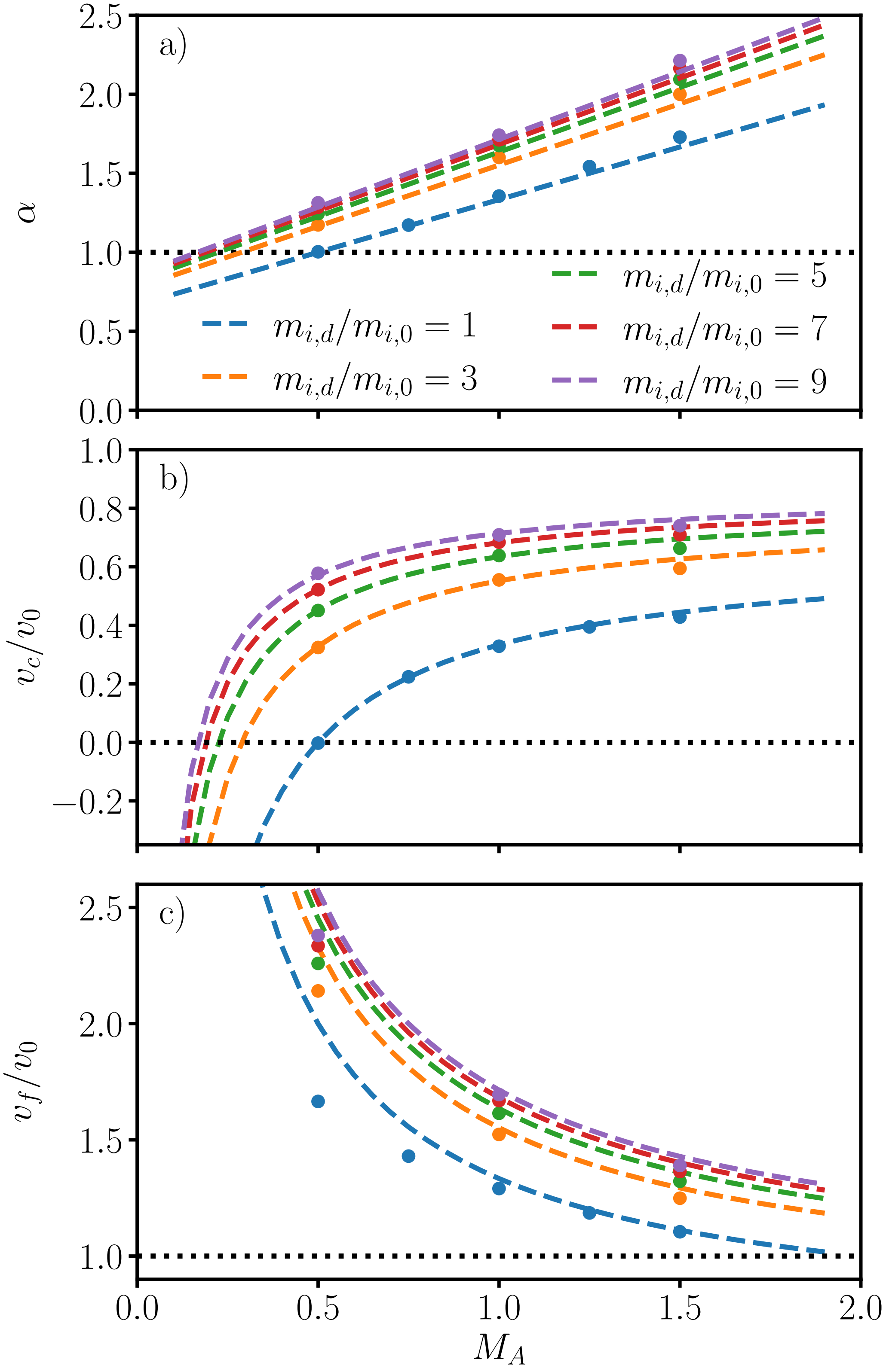
a)
b)
c)
α
v_c/v_0
v_f/v_0
M_A
$m_{i,d}/m_{i,0} = 1$
$m_{i,d}/m_{i,0} = 3$
$m_{i,d}/m_{i,0} = 5$
$m_{i,d}/m_{i,0} = 7$
$m_{i,d}/m_{i,0} = 9$
0.0
0.5
1.0
1.5
2.0
2.5
0.2
0.4
0.6
0.8
−0.2

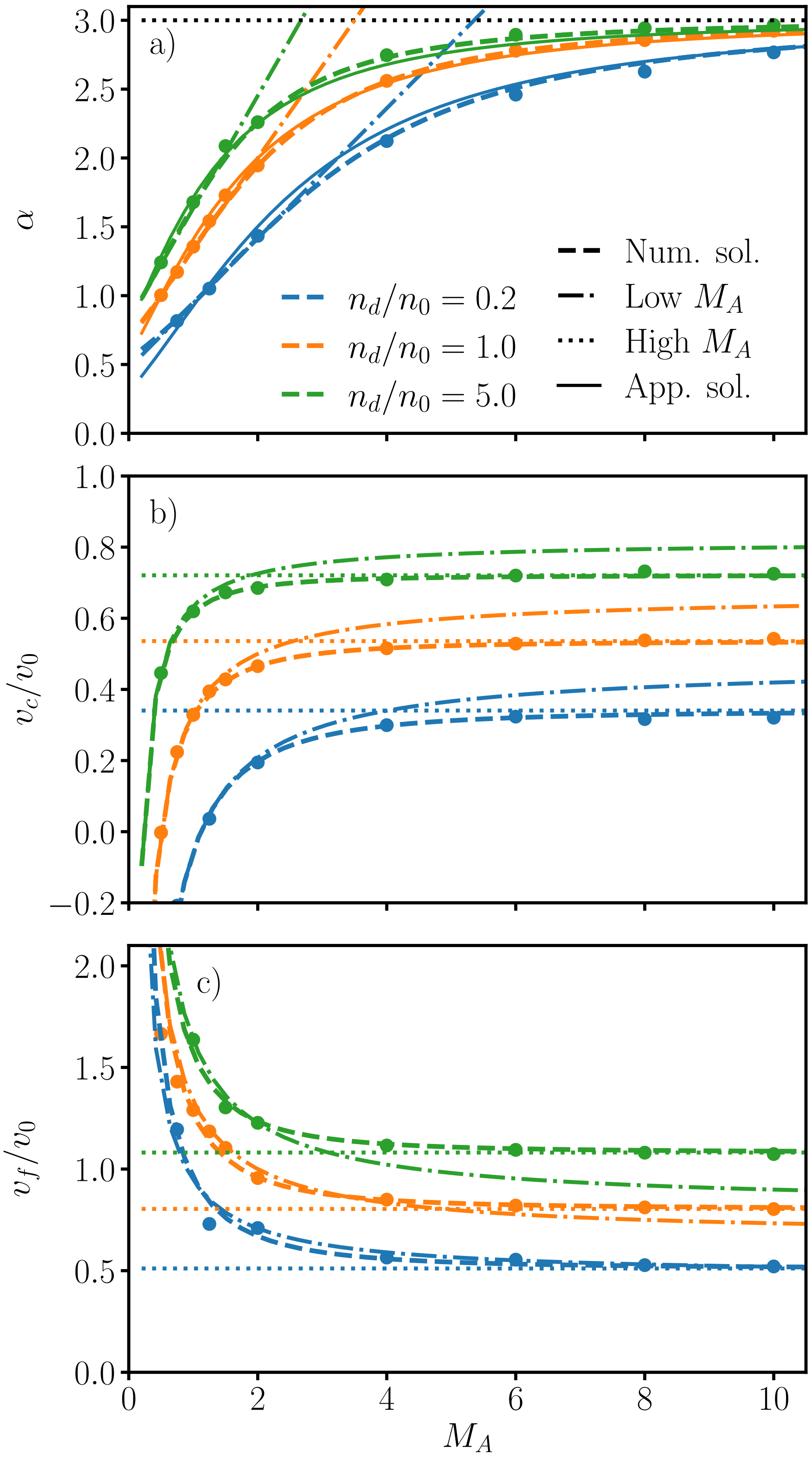
a)
α
3.0
2.5
2.0
1.5
1.0
0.5
0.0
Num. sol.
Low M_A
High M_A
App. sol.
$n_d/n_0 = 0.2$
$n_d/n_0 = 1.0$
$n_d/n_0 = 5.0$
b)
v_c/v_0
1.0
0.8
0.6
0.4
0.2
0.0
−0.2
c)
v_f/v_0
2.0
1.5
1.0
0.5
0.0
0
2
4
6
8
10
M_A

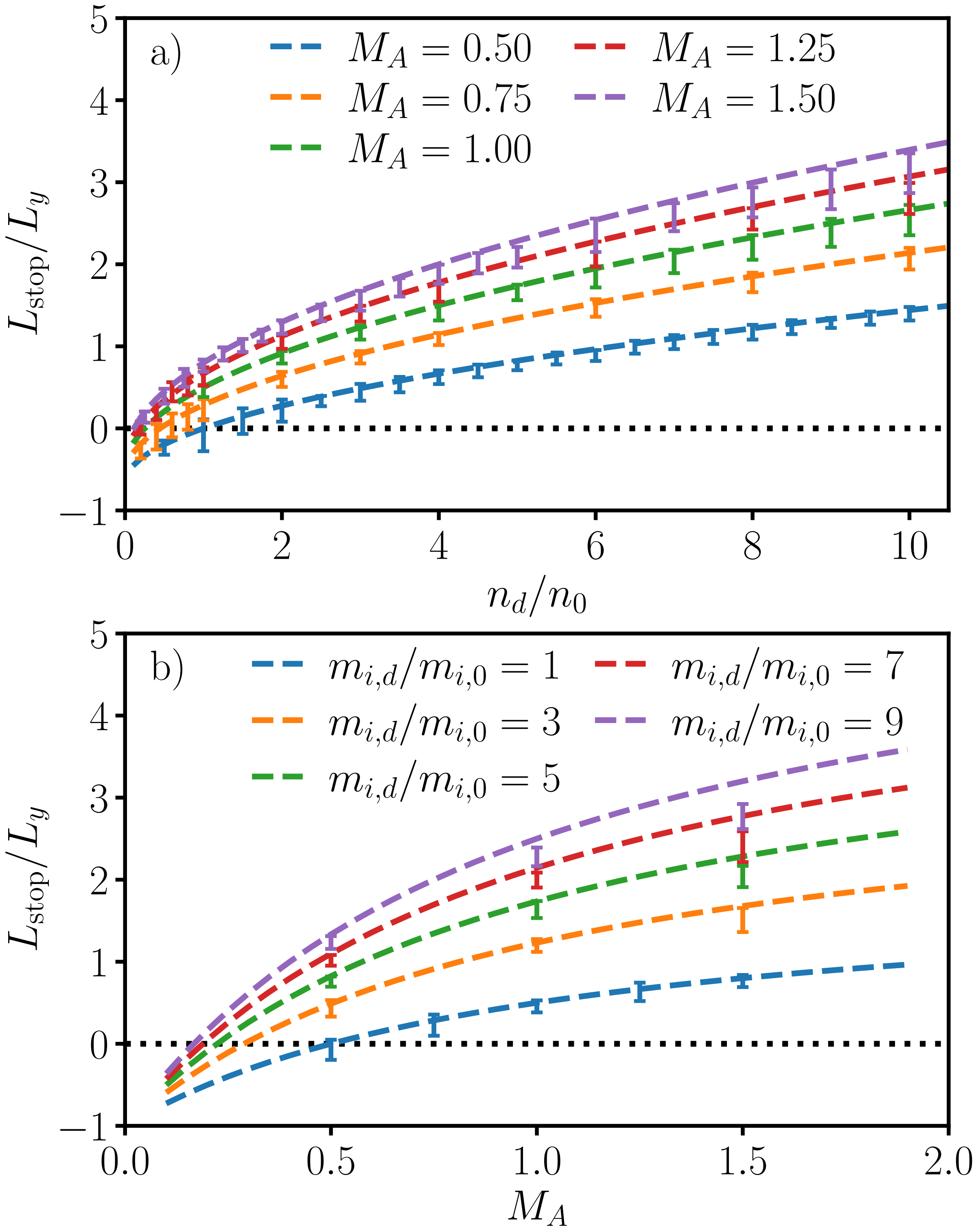
a)
$M_A = 0.50$
$M_A = 0.75$
$M_A = 1.00$
$M_A = 1.25$
$M_A = 1.50$
$L_{\rm stop}/L_y$
n_d/n_0
−1
0
1
2
3
4
5
0
2
4
6
8
10
b)
$m_{i,d}/m_{i,0} = 1$
$m_{i,d}/m_{i,0} = 3$
$m_{i,d}/m_{i,0} = 5$
$m_{i,d}/m_{i,0} = 7$
$m_{i,d}/m_{i,0} = 9$
$L_{\rm stop}/L_y$
M_A
0.0
0.5
1.0
1.5
2.0

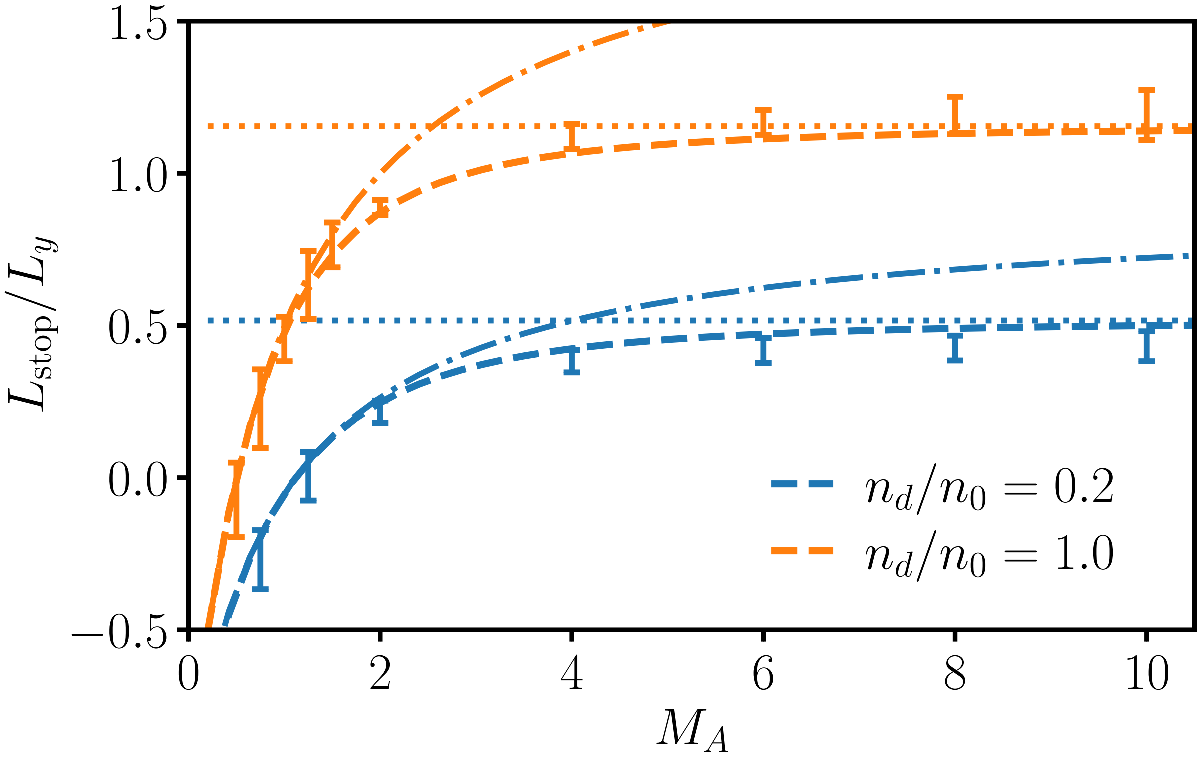
L_{stop}/L_y
1.5
1.0
0.5
0.0
−0.5
0
2
4
6
8
10
M_A
$n_d/n_0 = 0.2$
$n_d/n_0 = 1.0$

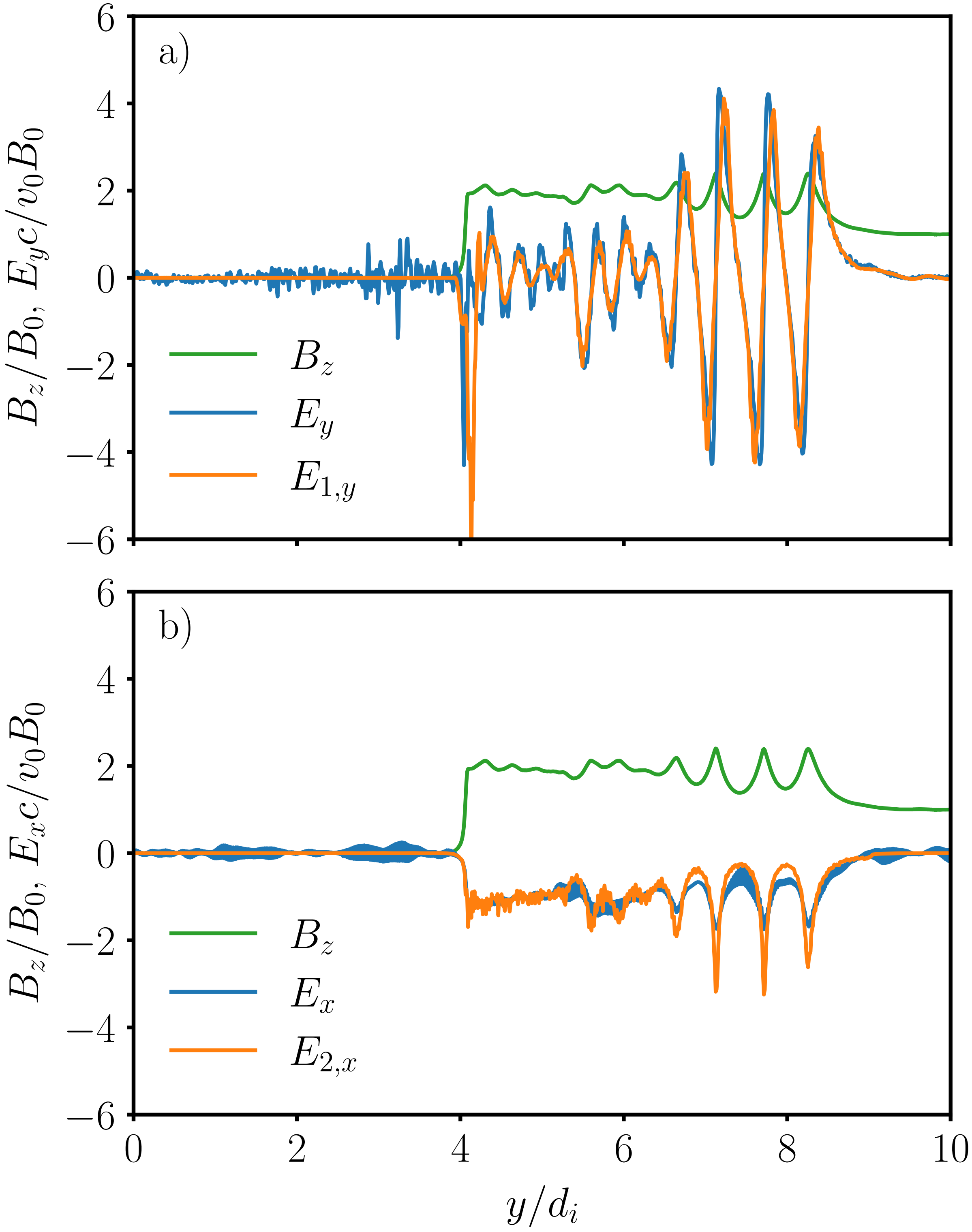
a)
b)
$B_z/B_0,\ E_y c/v_0 B_0$
$B_z/B_0,\ E_x c/v_0 B_0$
B_z
E_y
$E_{1,y}$
B_z
E_x
$E_{2,x}$
6
4
2
0
−2
−4
−6
0
2
4
6
8
10
y/d_i

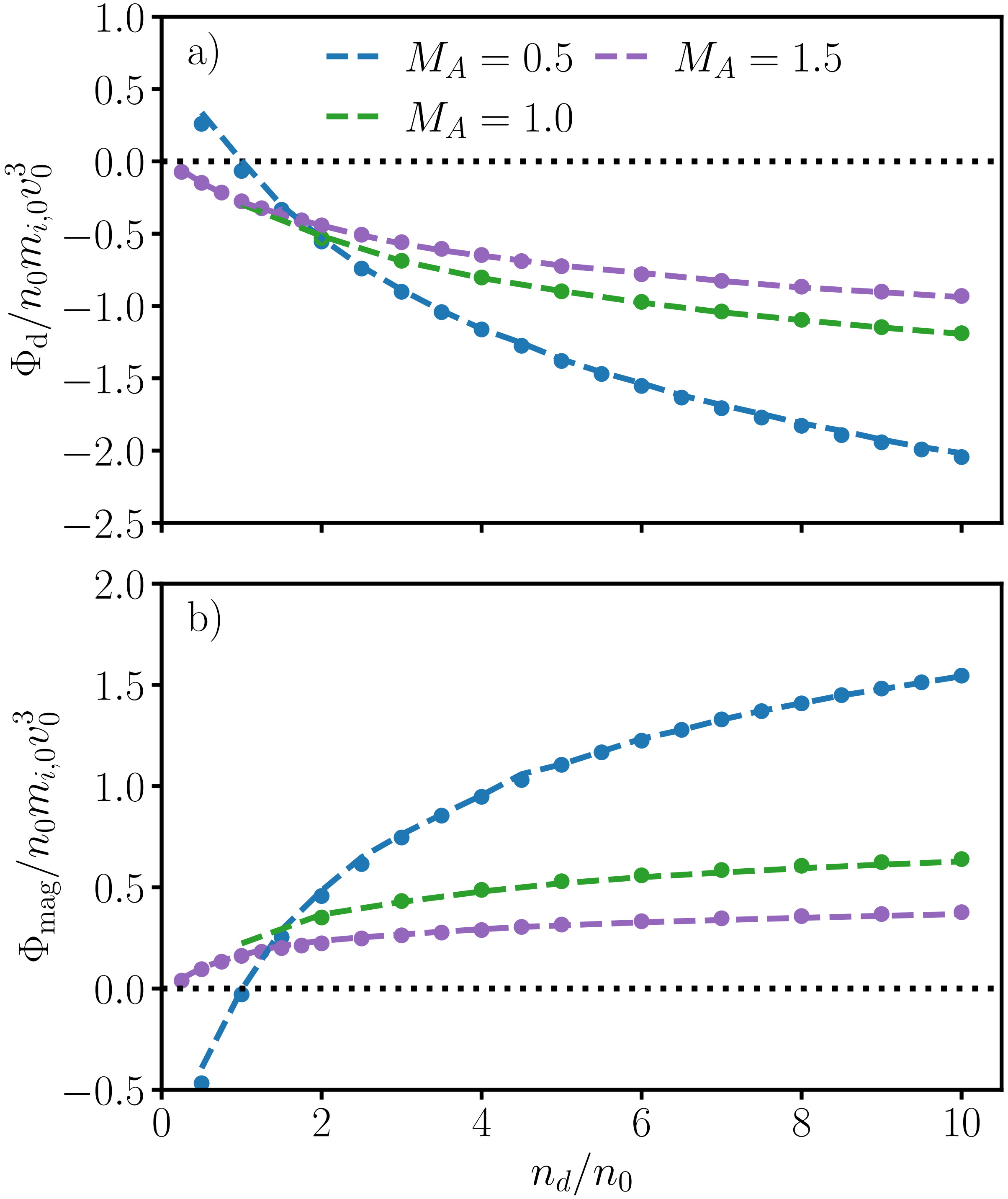
a)
$M_A = 0.5$
$M_A = 1.5$
$M_A = 1.0$
$\Phi_{\rm d}/n_0 m_{i,0} v_0^3$
1.0
0.5
0.0
−0.5
−1.0
−1.5
−2.0
−2.5
b)
$\Phi_{\rm mag}/n_0 m_{i,0} v_0^3$
2.0
1.5
1.0
0.5
0.0
−0.5
0
2
4
6
8
10
n_d/n_0

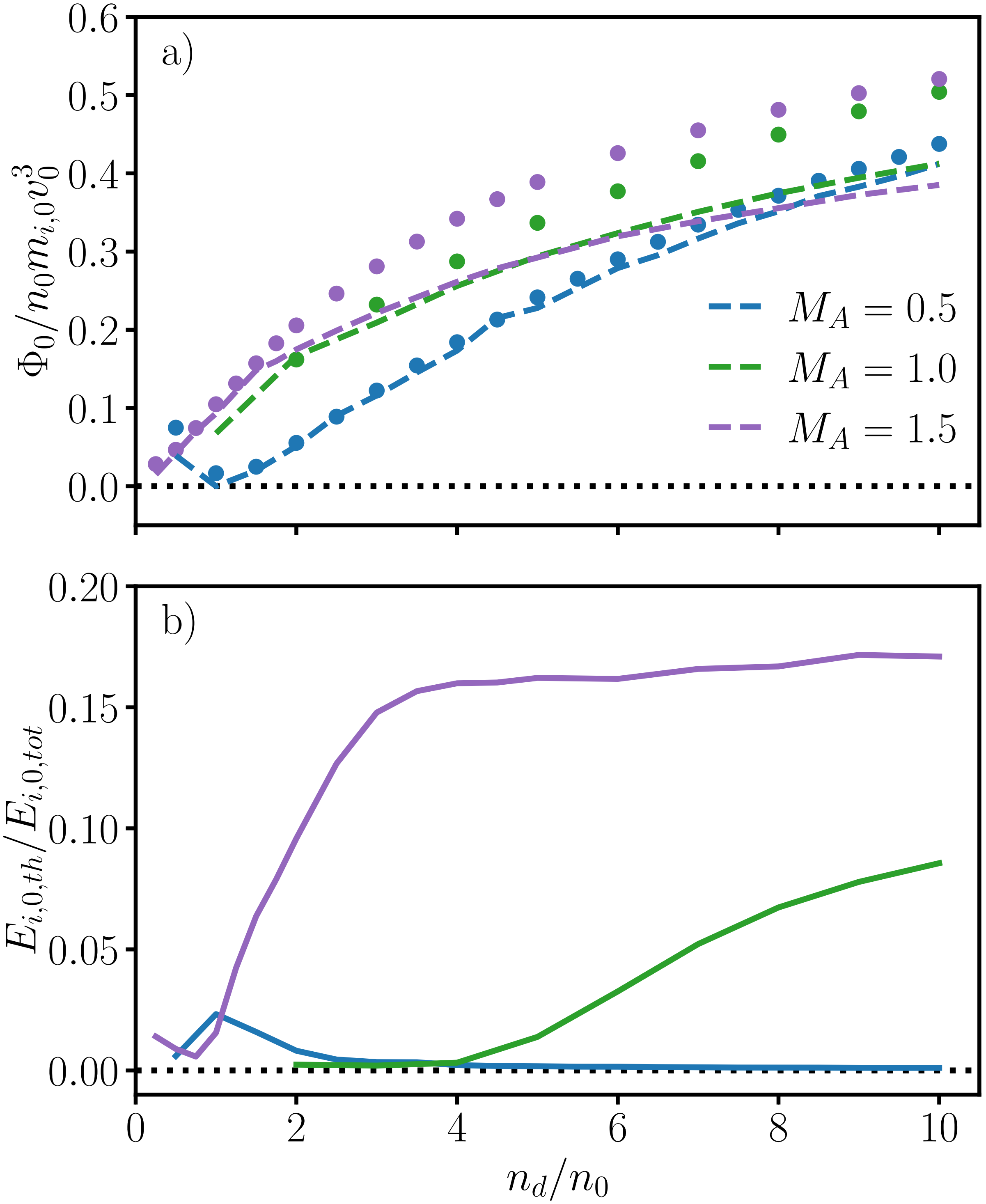
a)
b)
$\Phi_0/n_0 m_{i,0} v_0^3$
0.6
0.5
0.4
0.3
0.2
0.1
0.0
$M_A = 0.5$
$M_A = 1.0$
$M_A = 1.5$
$E_{i,0,th}/E_{i,0,tot}$
0.20
0.15
0.10
0.05
0.00
0
2
4
6
8
10
n_d/n_0